Argonne NATIONAL LABORATORY

ANL-21/69

Separation and Purification of Mo-99 Produced from Natural U_3O_8 Targets Via Photo-Fission

Chemical and Fuel Cycle Technologies Division

ANL-21/69

Separation and Purification of Mo-99 Produced from Natural U_3O_8 Targets Via Photo-Fission

by
M. Alex Brown[1], Yana Karslyan[1], Anna Servis[1], Andrei Patapenka[2], Roman Gromov[2], Joshua Hlavenka[2], Kurt Alford[2], Sergey Chemerisov[2], and Peter Tkac[1]

[1]Chemical and Fuel Cycle Technologies Division, Argonne National Laboratory
[2]Experimental Operations and Facilities Division, Argonne National Laboratory

December 2021

CONTENTS

CONTENTS (Cont.)

FIGURES

FIGURES (Cont.)

TABLES

ACRONYMS

AHA	acetohydroxamic acid
ALARA	as low as reasonably achievable
AMIPA	American Medical Isotope Production Act
AgZ	silver mordenite (zeolite)
EOB	end of bombardment
EPDM	ethylene propylene diene monomer
FWHM	full width at half maximum
HDEHP	di-2-ethylhexyl phosphoric acid
HEU	high-enriched uranium
HSA	high-specific activity
HPGe	High-Purity Germanium
LEAF	Low-Energy Accelerator Facility at Argonne National Laboratory
LEU	low-enriched uranium
LINAC	electron linear accelerator
MCNP	Monte Carlo N-Particle code
MoLLE	Molybdenum Liquid-Liquid Extraction
NO_x	Nitrogen oxide
OTR	Optical Transition Radiation
TBP	tributyl phosphate
UHP	ultra-high purity
UREX	Uranium Extraction

1 INTRODUCTION

The most-used medical isotope is ^{99m}Tc ($t_{½}$ = 6.0 h), which comprises over 80% of isotopes used in nuclear medicine today. It is normally derived from its transient equilibrium parent ^{99}Mo ($t_{½}$ = 66 h). A recent surge of interest in using the more proliferation-resistant low-enriched uranium (LEU) under the American Medical Isotope Production Act (AMIPA) has presented this technical challenge: can a domestic supplier meet the estimated weekly U.S. demand of 1500 6–day Ci of ^{99}Mo?

Superconducting electron linear accelerators (LINACs) with high-Z converter targets can generate bremsstrahlung photons and neutron fluxes that can induce photonuclear reactions and LEU fission.[1] A particular advantage of this utility is that it does not rely on high-enriched uranium (HEU)-fueled reactor cores (which are currently slated for LEU conversion) and can operate on an almost continuous basis. After sufficient production intervals, targets can be rotated out and processed while another batch is irradiated. Although ^{99}Mo production rates are lower than conventional reactor channels, the continuous operation capability of electron accelerators, combined with lower costs, reduced waste generation, and their proliferation-resistant nature renders this technology competitive.

Regarding the chemical processing and purification of ^{99}Mo from irradiated uranium targets in acidic solutions, the benchmark procedure is known as the Cintichem process or modifications thereof with respect to the use of LEU. The process relies on multiple precipitation, filtration, and column purification steps. It is also important to note that the Cintichem process prescribes the addition of stable Mo to carry ^{99}Mo on alpha-benzoin oxime, which reduces the specific activity of ^{99}Mo (curies of ^{99}Mo per gram of total Mo). Although this practice may be sufficient for large batches of ^{99}Mo (>1000 Ci), it could be problematic for smaller-scale processes that pursue the rapid distribution of hundreds of Ci or less. Conventional alumina-based generators are strongly dependent on the specific activity of ^{99}Mo and increasing concentrations of Mo will increase the column size and ultimately decrease the concentration of the ^{99m}Tc-saline product.[2]

Our goal was to develop and experimentally demonstrate a new chemical purification process that could quickly treat irradiated uranium targets for the recovery of high-specific activity (HSA) ^{99}Mo within several hours. To be viable, the procedure must fulfill the following requirements: (1) rapid execution with minimal time-consuming precipitation and filtration steps, (2) no addition of stable carrier elements so as to not subvert the high-specific activity of valuable fission products, and (3) a method that is mindful of the need to recover LEU target material. To facilitate these requirements, we derived a separation scheme that relies primarily on solvent extraction. This approach results in excellent front-end removal and back-end recovery of uranium in dilute acids (UREX — Uranium Extraction). Second, the solvent extraction of Mo by an organophosphoric or phosphonic acid from mild nitric acids (MoLLE — Molybdenum Liquid-Liquid Extraction) is capable of decontaminating Mo from a mixture of fission products born out of a UREX raffinate. Similar process chemistry was recently used to selectively remove Mo during the recovery of minor actinides in spent nuclear fuel. The major advantage of this combined approach (UREX + MoLLE) includes the potential to execute these

process stages using a continuous flowsheet with equipment such as high-throughput-counter-current centrifugal contactors without the need for time-consuming precipitation and filtration steps. For final purification, an anion-exchange column yields low-volume, high-specific activity $^{99}MoO_4^{2-}$ in a simple alkaline matrix. This platform can also be used to concentrate multiple batches. This process was first reported in 2020.[3]

To support the purification and recovery of HSA ^{99}Mo, there are other critical components to address that ensure efficient process operations. Noble gas isotopes of Xe, Kr, and to some extent I, can be fractioned from an untreated irradiated uranium pellet; their removal without any chemical treatment should be analyzed. The dissolution of uranium is an important factor as well, as the co-evolution of nitrogen oxide (NO_x) and volatile fission gases. The equilibrium concentration of nitric acid must be within a specific window in order to facilitate U(VI)-TBP (tri-n-butyl phosphate) extraction without pH control. Consequently, the dissolution of U_3O_8 must be performed with a specific volume and initial concentration of nitric acid. Time is also an essential factor and the time required for target dissolution must be optimized to avoid decay losses. Similarly, isotopes of iodine are notoriously volatile in nitric acid and must be managed and/or trapped during front-end processing.

This work describes our investigation of six major steps in the treatment of photon-irradiated U_3O_8 targets. They are (1) targetry and simulations, (2) noble gas removal, (3) target dissolution, (4) removal of gaseous and iodine speciation, (5) solvent extraction and ion exchange, and (6) quality assurance and control of the ^{99}Mo product. Three irradiations were performed in FY2021 comprising 1.5 kW*h, 2.9 kW*h, and 30.1 kW*h on a 5.8-g $^{nat}U_3O_8$ pellet provided by Niowave, Inc.

2 EXPERIMENTAL

2.1 TARGET CONFIGURATION

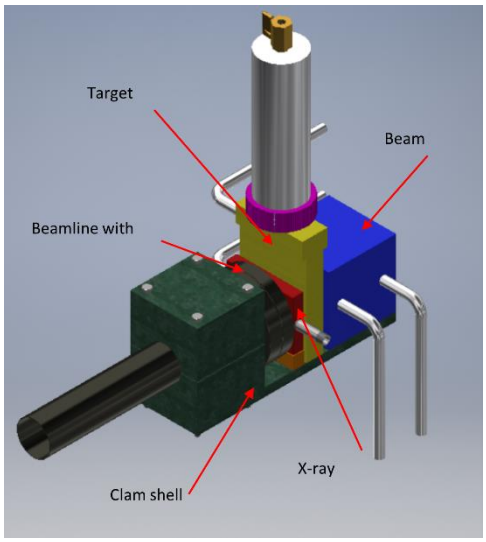

FIGURE 1 Experimental setup used for irradiation of uranium oxide pellets

For irradiation of U3O8 uranium oxide pellets, we designed a dedicated irradiation system. The system consists of aluminum clamshell support, a high-Z (Ta) converter, target holder, and beam stop (FIGURE 1). The X-ray converter, target holder, and beam stop are cooled with water flow. Each of the components has its own dedicated water source due to different cooling requirements. The X-ray converter adsorbs most of the beam and requires a high flow rate, while the target holder and the beam stop have significantly lower heat deposition and require lower water flow. The X-ray converter consists of an aluminum shell housing containing six 0.5-mm-thick Ta disks separated by a 1-mm gap for water flow. The maximum design power for this converter is 3 kW. The target housing consists of multiple layers to ensure the containment of volatile fission gases. Primary containment (FIGURE 2) consists of the aluminum tube — housing a uranium oxide pellet — connected to the second tube with the valve.

The connection between the tubes is sealed with an ethylene propylene diene monomer (EPDM) gasket. The valve allows evacuation and leak-checking of the containment and collection of the fission gases after irradiation. The primary containment is inserted into the aluminum body. There is a 1-mm gap between the tube and the body for cooling water flow. The secondary enclosure is formed by a 7.5-cm-diameter tube attached to the water-cooled body and sealed with an EPDM gasket. There is a valve mounted on top of the tube that allows for leak check of the secondary containment and collects gases from the secondary containment after each irradiation.

To ensure integrity of the primary and secondary containment, we have leak-checked containments according to the following procedure (FIGURE 2). First, a uranium oxide pellet was placed inside the sample tube, and the sample tube was closed and connected to the valve. The internal volume of the primary containment was connected to the helium leak detector. The primary containment was sprayed with helium and if no leak was detected, we proceeded to the next step. Next, the valve was closed, and an ultra-high purity (UHP) helium cylinder was attached to the valve and the primary containment was filled with gas. Helium has high thermal conductivity, which facilitates target cooling during irradiation. After this, we closed the valve and installed the secondary containment (FIGURE 3 and FIGURE 4). We repeated the same leak-checking procedure for the secondary containment.

FIGURE 2 Primary containment during leak-checking

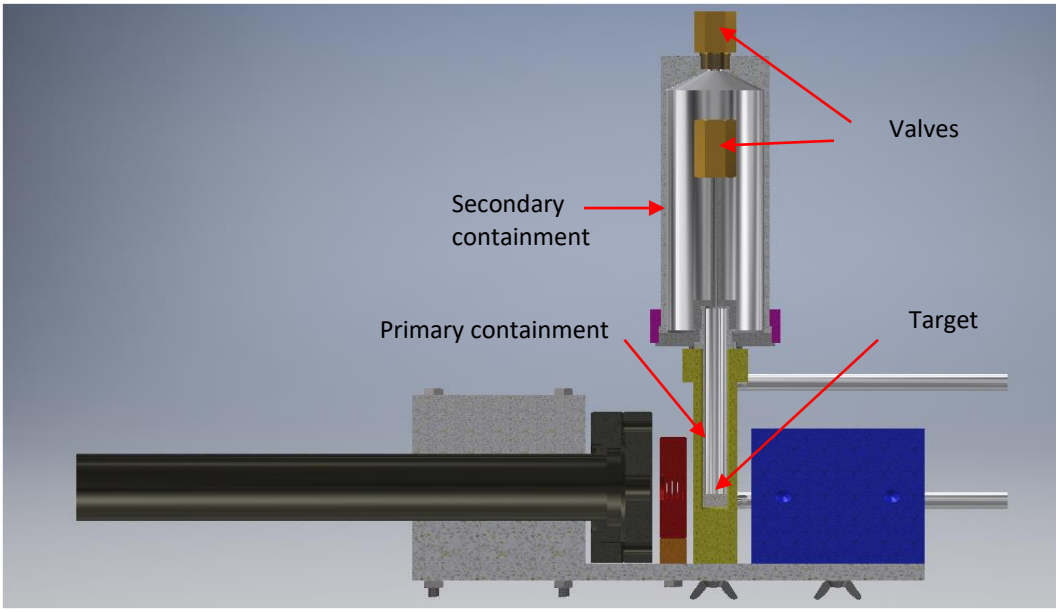

FIGURE 3 Cross-section of the irradiation setup

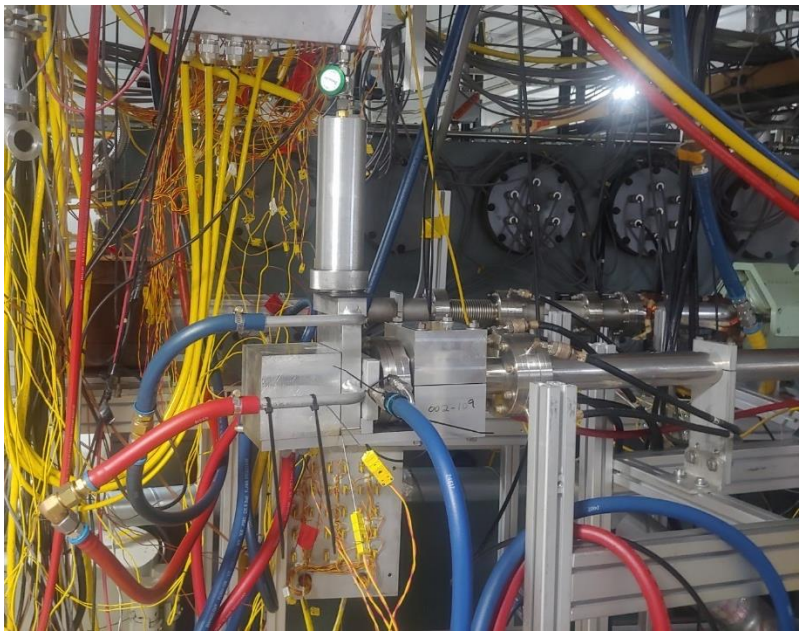

FIGURE 4 Irradiation setup installed at the end of the beamline

2.2 IRRADIATIONS

We performed three irradiations of the uranium oxide pellet, irradiating a single ~5 g pellet in each experiment. All irradiations were performed at 40 MeV beam energy. Beam power

for the first irradiation was limited to 1.5 kW. The second and third irradiations were conducted at 3 kW beam power. TABLE 1 summarizes the irradiation parameters.

TABLE 1 Summary of Irradiation Parameters

Irradiation	Date of irradiation	Beam energy, MeV	Beam power, kW	Duration, hours	Total energy, kW×h	Beam size, FWHM mm
1	08/09/2021	40	1.6	1	1.6	9×10
2	08/30/2021	40	3	1	3	7.6×7.7
3	09/24/2021	40	2.7	11	30.1	9.2×9

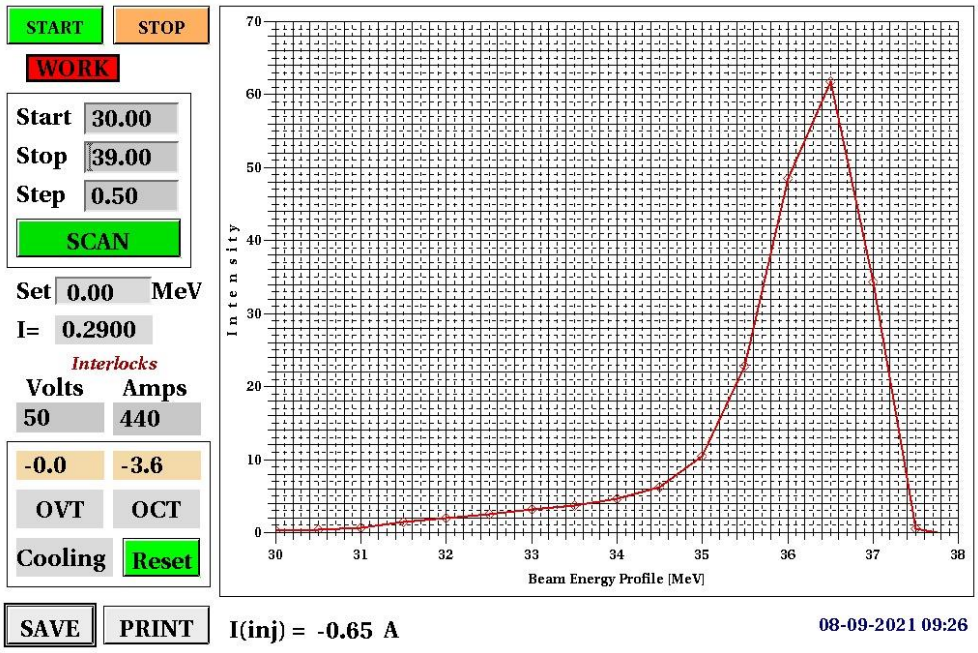

FIGURE 5 Beam energy spectrum recorded at peak energy of 36.5 MeV; after optimization, we decreased beam current to shift beam energy to 40 MeV

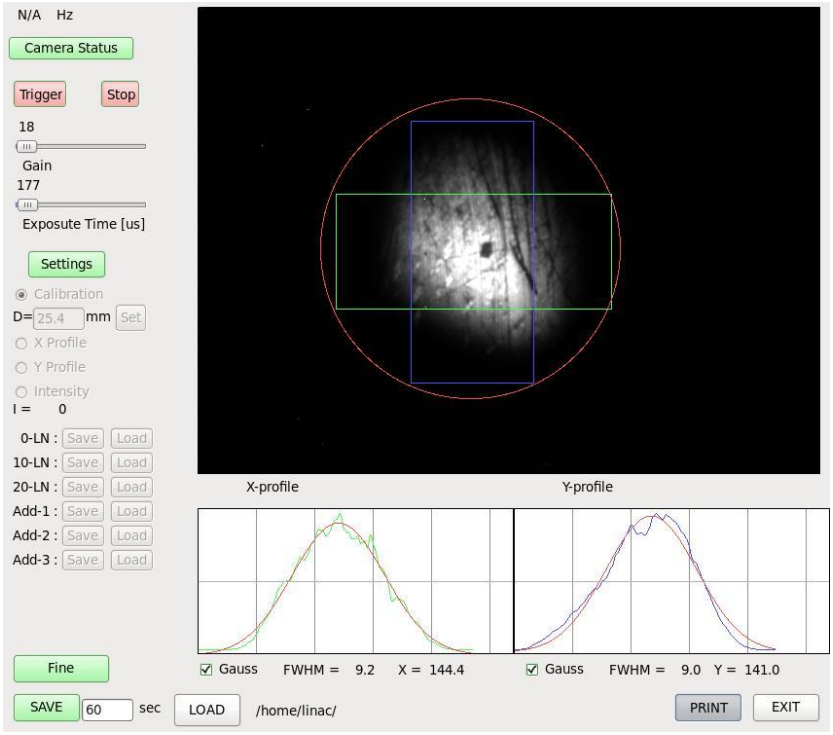

FIGURE 6 Optical Transition Radiation (OTR) signal from the beam placed on the front face of the beam stop

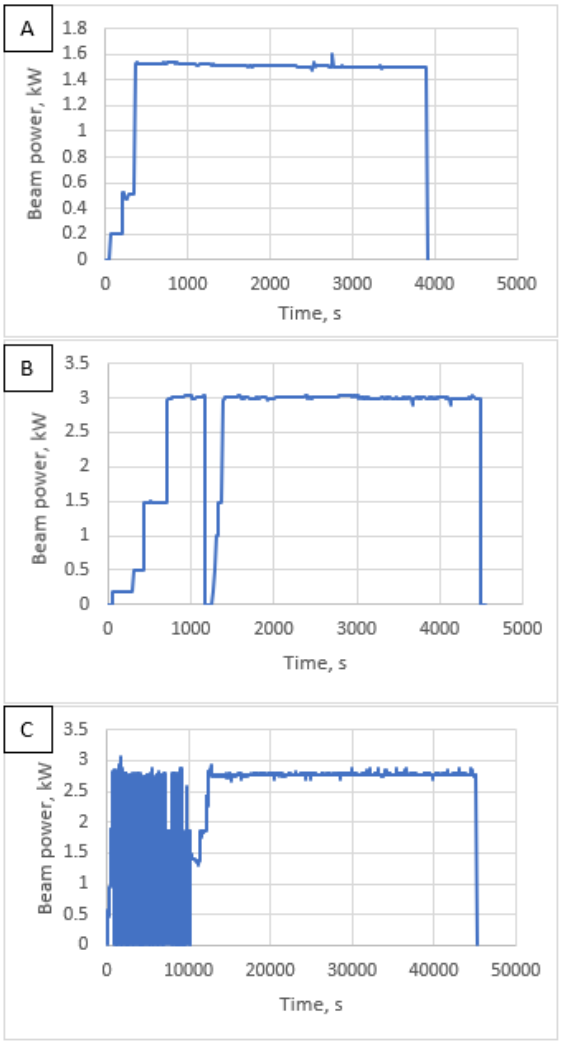

FIGURE 7 Beam history for all three irradiations: A-irradiation #1, B-irradiation #2, and C-irradiation #3

We tuned the beam transport system the day prior to irradiation, and verified the beam parameters on the day of irradiation. Due to limitations for heat dissipation in the spectrometer magnet, the energy spectrum was measured at 38 MeV. FIGURE 5 presents an example of the typical energy spectrum. After spectrum acquisition, we reduced the peak beam current to shift the beam energy peak to 40 MeV. After energy verification, the beam was transported to the end of the beamline and through the water-cooled beryllium window to the aluminum beam stop, and the beam shape was adjusted to produce a ~9×9 mm full width at half maximum (FWHM) beam spot on the beam stop (FIGURE 6). After this, we installed the target holder and connected the water lines. Typically, irradiation is stated at low ~200W beam power, and power was increased until desired beam power is reached. Beam histories for all three irradiations are shown in FIGURE 7.

We removed the first two irradiation samples the following day. For the last irradiation, we allowed a 2.5-day cooldown due to excessively high radiation doses from ^{24}Na near the target. After removing the target, we transferred it to the radiological laboratory for processing and analysis.

2.3 CHEMICAL PROCESSING

2.3.1 Reagents

We prepared organic solutions with either >99% tributyl phosphate (TBP) (Sigma-Aldrich) or 97% di-2-ethylhexyl phosphoric acid (HDEHP; Sigma-Aldrich) and 99+% n-dodecane (Alfa Aesar). We used deionized (DI) water with a resistivity of 18.2 MΩ·cm to prepare all aqueous solutions. Other reagents used include trace-element-grade concentrated nitric acid (Fisher Scientific); trace-element-grade concentrated hydrochloric acid (Fisher Scientific); oxalic acid dihydrate (certified ACS, Sigma Aldrich); sodium chloride (>99%, Sigma-Aldrich); 50% NaOH in water (Sigma Aldrich); acetohydroxamic acid (AHA; 98%, Acros Organics); sodium nitrate (99+%, Alfa Aesar); and concentrated ammonium hydroxide (ACS reagent, Fisher Scientific). The safety traps were filled with Drierite drying agent and silver mordenite (AgZ).

2.3.2 Solvent Extraction and Ion Exchange Column

Overview of the Process. The primary separation stages to recover and purify ^{99}Mo are shown in FIGURE 8. Following target dissolution and volatile isotope capture, the uranyl solution (of approximately 1.3M UO_2^{2+} and ~2.5M HNO_3) can be brought into contact with multiple stages of TBP in a hydrocarbon diluent. This removes the bulk uranium from nitric acid solution. Second, the solvent extraction of Mo by HDEHP from mild nitric acids (MoLLE – Molybdenum Liquid-Liquid Extraction) is capable of decontaminating Mo from a mixture of fission products born out of a UREX raffinate. Similar process chemistry was recently used to selectively remove Mo during the recovery of minor actinides in spent nuclear fuel.[4] The major advantage of this combined approach (UREX + MoLLE) includes the potential to execute these process stages using a continuous flowsheet with equipment such as high-throughput counter-current centrifugal contactors. For a final purification, an anion-exchange column yields low volume, high-specific activity ^{99}Mo in a simple alkaline matrix.

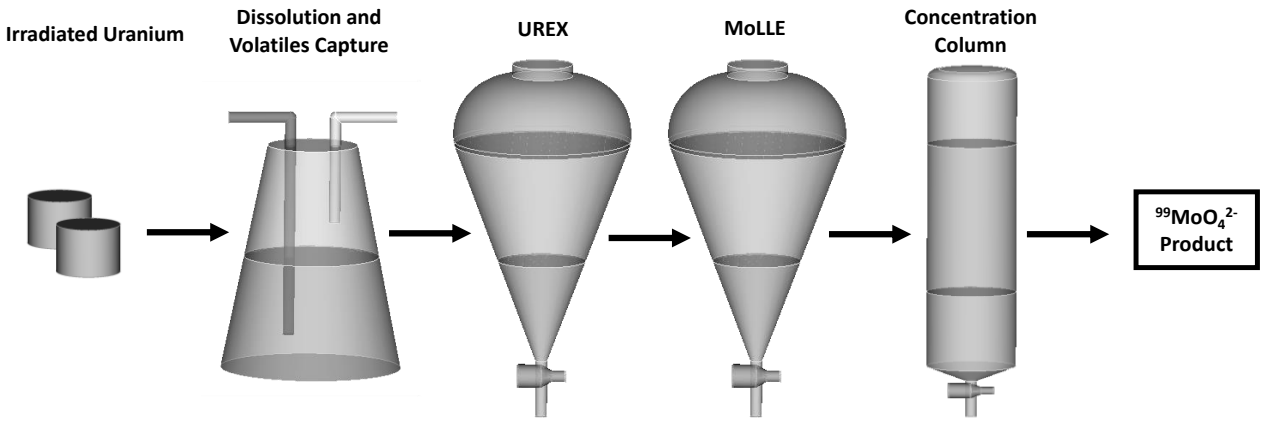

FIGURE 8 Stages of chemical separations to recover ^{99}Mo from irradiated uranium targets

Target Dissolution. After retrieving the target and removing the outer layers of containment, we evacuated the gases into primary and secondary gas cylinders and counted. The target was dissolved in the desired HNO_3 concentration (described in more detail below) with or without mixing and a slightly negative pressure at 77°C. The dissolution setup comprised the vessel, two 1M NaOH traps, one n-dodecane trap (optional), a Drierite trap, and an AgZ trap (FIGURE 9). The setup for the processing of target #1 (for irradiation #1) included an apparatus for distillation of the solution of dissolved target, while the setup for irradiations #2 and #3 did not incorporate distillation. For irradiations #2 and #3, the bubbling of traps was accompanied by periodical sample withdrawal from both NaOH traps (~0.2-0.3 mL of each) that were counted.

The dissolution of U_3O_8 in nitric acid can be described by the equilibrium:

$$U_3O_8 + 8HNO_3 \rightarrow 3UO_2(NO_3)_2 + 4H_2O + yNOx \quad (1)$$

where NO_x indicates the evolution of nitrous and nitrogen oxides. Since U_3O_8 and U_3O_7 can contain uranium valence states of (IV), (V), and (VI), a dark green color was observed in the initial stages of dissolution that was likely due to the presence of U(IV).[5] Complete dissolution is indicated by the bright yellow color of uranyl. To ensure a proper feed into the solvent extraction suites following dissolution (UREX + MoLLE), the equilibrium nitric acid concentration should be between 2M and 3M after dissolution. For 5.8 g of U_3O_8, approximately 17 mL of 6M HNO_3 should satisfy this requirement. The variables to influence the dissolution speed included temperature, agitation, and distillation.

The reaction vessel comprised a 50-mL round-bottom, three-neck flask. One port was designated for HNO_3 injection, another for air-intake, and the third port fed into the NaOH traps. We heated the flask using a calibrated heating mantle. The hydroxide traps comprised two gas-scrubbing bottles with 50 mL of 1M NaOH. Following the traps was a gas-washing bottle containing ~100 g of indicator Drierite, which was followed by another gas-washing bottle containing Drierite and silver zeolite. The system operated under a slight vacuum.

FIGURE 9 Setup for chemical processing after irradiation #1

Solvent Extraction. When the dissolution was complete, we removed the uranyl solution from the dissolution vessel. We took an aliquot of the solution to count the total production of isotopes. For irradiations #2 and #3, we took an aliquot of the dissolved target for iodine speciation test. Then, we withdrew two major samples of uranyl nitrate solution, followed by an H2O rinse of the dissolution flask to remove some undissolved solids and residual uranyl solution. The first batch of uranyl nitrate solution was chemically processed through UREX, MoLLE processes, and column elution. For the UREX process, we brought the solution of uranyl nitrate into contact with three rounds of 30% TBP (v/v) in n-dodecane for 45 seconds to remove the bulk uranium. The first two contacts comprised an O:A of 4:1.5 and the third of 1:1. Then for the MoLLE process, the raffinate was brought into contact with three rounds of 0.4M HDEHP. The first two contacts comprised an O:A of 1:2 with the UREX raffinate and the third approximately 1:6 to clean the interface. We then stripped the Mo from the loaded HDEHP using three contacts of 0.5M AHA and adjusted to pH~12 using concentrated NH4OH. For irradiation #3, we introduced one additional scrub stage during the MoLLE extraction, a contact with 3M HNO3.

Column. The concentration column comprised 1.0 g of AG 1-X8 (Millipore Sigma) in a 1 cm×10 cm non-jacketed, chromatography column that was pre-equilibrated with concentrated NaOH to transform the resin from Cl- to OH- form. The column was packed and washed with 1M NaOH, followed by the AHA strip solution containing ^{99}Mo and fission products. We washed the column with various concentrations of NaOH, HCl, oxalic acid, NaCl, or mixtures thereof described in a corresponding section 3.5. We then performed spectroscopy of all radiochemical samples using an ORTEC GEM series High-Purity Germanium (HPGe) detector.

2.3.3 Extraction Procedure for Iodine Speciation

First, we brought an aliquot of dissolved target solution containing ^{131}I into contact with an equal volume of toluene. We placed the two-phase mixture into a vortex mixer for 5 minutes and then centrifuged it for 5 minutes to separate phases. We repeated the step twice to completely remove I_2.

Second, we brought the remaining aqueous phase into contact with an equal volume of 0.1M I_2 in toluene to establish isotopic equilibrium between the natural I_2 (at a far larger concentration) and the radioiodine present as I^-. The fraction of the radioiodine that was present in the aqueous solution as I^- transfers to the organic phase with the I_2 due to isotopic exchange with the far larger mass of natural iodine. We placed the two-phase mixture into a vortex mixer for 5 minutes and then placed it in a centrifuge for 5 minutes, and repeated this step three times. The activity remaining in aqueous phase was IO_3^-. We brought all organic phases into contact with an equal volume of 0.1M $Na_2S_2O_3$ in 0.1M NaOH to reduce any volatile I_2 to nonvolatile I^- prior to gamma counting.

2.3.4 Thiocyanate Extraction (QC Procedure)

Preparation of Solutions Used in Thiocyanate Extraction. To prepare the fission product carrier, we transferred 10 mg of $RhCl_3 \cdot 3H_2O$ into a flask containing 50 mL of water, acidified with 1 mL of 70% HNO_3, and mixed it until fully dissolved. We then added 11 mL of 70% HNO_3 to a beaker containing 5 mL of water, then added 10 mg of K_3RuCl_6 and mixed that in until fully dissolved. Then, we dissolved 500 mg of MoO_3 in 20 mL of 1M NaOH and acidified that with 2 mL of 4M HNO_3. After combining Rh, Ru, and Mo solutions in a volumetric flask, we diluted them to 200 mL with water.

For the purpose of pre-equilibration of ethyl acetate, we prepared and mixed a solution containing 0.33 mL of 0.1M NaOH combined with 3.33 mL of 10% H_2SO_4. We added 167 µL of $Fe_2(SO_4)_3$ (10 mg Fe/mL) in 1% H_2SO_4 and mixed that, followed by 0.33 mL of 50% NH_4SCN in water and further mixing. Then we added and mixed 0.83 mL of 10% $SnCl_2$ in 10% HCl. We then combined the solution with 20 mL of ethyl acetate and mixed it for 1 minute in a vortex mixer. The phases were separated by centrifugation and we used the ethyl acetate the same day.

The Extraction Procedure. First, we preequilibrated 6 mL ethyl acetate with the aqueous phase described above. Then, to prepare for extraction, we combined 0.4 mL of the ^{99}Mo product with 0.04 mL of Rh/Ru/Mo carrier solution, 4 mL 1.8M H_2SO_4, 0.4 mL 6.6M NH_4SCN, 1 mL 0.44M $SnCl_2$ in 1.2M HCl, and 0.2 mL 0.075M $Fe_2(SO_4)_3$ in 0.18M H_2SO_4. We brought this solution into contact with 5 mL, then 2 mL, of the preequilibrated ethyl acetate. We removed and discarded the organic phase following each contact. We then collected a 4-mL sample of the aqueous phase for overnight gamma counting in a well-type HPGe detector.

2.3.5 Iodine Extraction (QC Procedure)

For the iodine procedure, we took a 0.1mL of Mo product in 1M NaCl and 1M NaOH for analysis. We performed extraction in a 20-mL glass scintillation vial, adding one drop of KI in water (10 mg I/mL) to 10 mL of water, followed by the addition of 0.1 mL of ^{99}Mo product solution (last eluate from the column). We then added one drop of 8M HNO_3 and combined the solution with 5 mL of $CHCl_3$. Then we added two drops of 35% HCl and four drops of 20% $NaNO_2$ in water and mixed that for 1 minute. The phases were allowed to separate, and we transferred the organic phase (bottom phase) into a new glass vial. Then we added two drops of 20% $NaNO_2$ in water to the aqueous phase, and combined the solution with 5 mL of $CHCl_3$ and mixed it for 1 minute. The phases were allowed to separate, and then transferred and combined the organic phase (bottom) with $CHCl_3$ from the first extraction step. We used the combined organic phase to determine the activity of ^{131}I using gamma counting.

2.4 GAMMA COUNTING

We performed gamma spectroscopy on aqueous samples to determine the produced activities of fission products at various points in solution processing. This information enabled us to quantify the recovery achieved by the various steps as well as the overall procedure, and to determine the points at which several important isotopes/contaminants were removed from the final product.

We used an Eckert & Ziegler mixed-isotope standard to complete our calibrations, as follows. First, we connected a coaxial geometry HPGe detector to ORTEC DSPEC 50 digital analyzers calibrated at various distances to accommodate samples of different strengths. We then mechanically cooled the instrument using an ORTEC X-COOLER III coupled to an autosampling system with a shielded canyon, where the sample resided for counting (FIGURE 10).

Sample Preparation and Analysis

Each stage of operation was aliquoted (dissolution, UREX, MoLLE, concentration column, QA/QC). We took an aliquot of a known weight from a known bulk solution and diluted it to 20 mL in a plastic scintillation vial to match the calibration standard geometry. Aqueous aliquots were diluted with water while extractants were diluted with dodecane. We sealed samples with parafilm, had them surveyed by health physics personnel, and submitted them for gamma analysis. We placed each sample at a distance that provided <3% detector dead time but allowed for sufficient counting statistics. The nuclides of interest with corresponding photopeaks are listed in TABLE 2.

TABLE 2 Peak Energies of Radionuclides Monitored During Chemical Processing

Radionuclide	Peak Energy (keV)
^{88}Kr	196.3
^{237}U	208.1
^{132}Te	228.5
^{135}Xe	249.8
^{239}Np	277.6
^{143}Ce	293.3
^{105}Rh	318.6
^{103}Ru	497.2
^{133}I	529.9
^{140}Ba	537.3
^{91m}Y	557.4
^{131}I	636.9
^{99}Mo	739.5
^{97}Zr	743.4
^{91}Sr	749.8
^{95}Zr	756.7
^{95}Nb	765.8
^{140}La	1596.4

FIGURE 10 Mechanically cooled coaxial detector coupled to an autosampling unit with a shielded canyon for counting

3 RESULTS AND DISCUSSION

3.1 DOSE RATES FOR THE IRRADIATED SAMPLES AND ACTIVITY LIMITS

We used the FLUKA Monte Carlo code[6] to calculate three-dimensional ambient dose equivalent rate maps for the irradiated samples in a transport container and activities limits for noble gas fission products. These predictions were considered for the design of experimental components and the transport container. The results will be used to assess the radiological impact — in terms of individual and collective dose — for typical interventions in the area and, thus, help in optimizing the experimental planning as required by the as low as reasonably achievable (ALARA) principle.

We performed a set of simulations before the experiments to estimate activity limits for specific isotopes ^{135}Xe and ^{85}Kr and shielding efficiency of a transport container. We assumed the irradiation scenario of 3-kW beam power for 40 hours (120kWh). Based on the results, expected activity at end of bombardment (EOB) is 135.9mCi of ^{135}Xe and and 6.6 mCi of ^{85}Kr.

We calculated ambient dose maps for the irradiated target two cases: three U pellets without (a) any shielding and (b) inside the transport container. We simulated the transport container as a cylindrical body with wall thicknesses of 2 inches and a height of 10 inches (FIGURE 11).

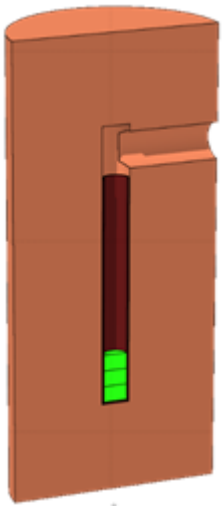

FIGURE 11 Simulation of U-pellets inside the transport container; Green region = Uranium samples, Light Brown region = Steel transport container, Dark Brown region = Uranium samples envelope (SS304 steel)

Average dose rates at 30-cm and 100-cm distances from the irradiated uranium target are shown in TABLE 3. Residual ambient dose maps for the samples shielded by the transport container are shown in FIGURE 12. The color scale threshold is given 1 mrem/h. As shown, the container reduces the dose rates by ~5–10 times.

Doses time decay law for the described cases can be represented by empirical formula:

$$Dose(T) = Dose(T_0) \times T^{-const} \quad (2)$$

where T is a cooling time expressed in hours and const is – dimensionless constant. The power law describes the dose decay very well in a time range of 1 hour–1 week. For shielded/unshielded cases, the constant is equal 0.744 and 0.691, respectively.

TABLE 3 Average Doses from Irradiated U-pellets

	Dose rates at 30 cm from the U-samples, mrem/hour		**Dose rates 100 cm from the U-samples, mrem/hour**	
Cooling time	**No shielding**	**Samples are inside the container**	**No shielding**	**Samples are inside the container**
1 hour	13294.9	2488.6	1191.7	220.9
1 day	1781.2	251.4	159.0	22.3
1 week	372.8	54.2	33.3	4.8
1 month	71.1	11.8	6.4	1.1

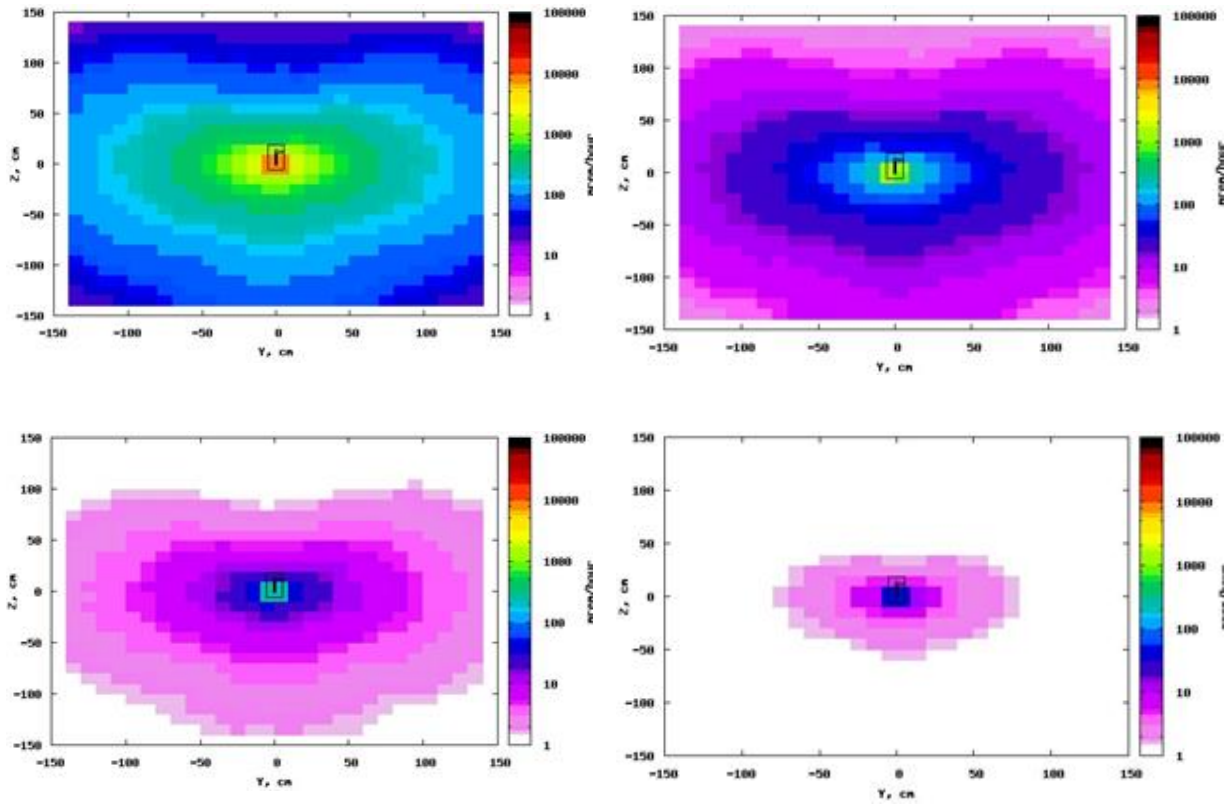

FIGURE 12 Residual doses distribution from U-samples inside the transport container — Cooling times: 1 hour (top left); 1 day (top right); 1 week (bottom left); 1 month (bottom right)

3.2 TOTAL PRODUCTION OF ISOTOPES: MONTE-CARLO SIMULATIONS

We performed Monte-Carlo simulations on each irradiation to assess production and compared the results were compared against experimental determinations. Discrepancies and potential sources of error are discussed below.

3.2.1 Simulation Procedure and Model of the Experimental Assembly

We performed a set of Monte-Carlo simulations in support of irradiations of U_3O_8 pellet to produce ^{99}Mo. We used the calculation results to estimate production inventory expected at the end of each irradiation and then compared those estimated values with measured values obtained via gamma spectroscopy.

The Monte Carlo model of U_3O_8 target assembly includes the following parts: beam window (Al6061 alloy); tantalum converter and the aluminum converter holder (Al6061 alloy); beam dump (volumetric mixture of Al6061 [90%] and water [10%]); beam pipe and the assembly interconnector (Al6061 alloy); flange (Al6061 alloy); and U_3O_8 pellet (natural enrichment on ^{235}U–0.72%); the pellet is in an He-filled primary container (316 stainless steel)

cooled by water, and then placed inside the secondary container's holder (Al6061 alloy). We prepared a pressed Uranium Oxide (U_3O_8) sample with a cylindrical form (H=8.88 mm, D=12.84 mm), density 5.08 g/cm^3 and natural uranium isotopes composition. We performed simulations for a single pellet located on the beam axis and for a stack of three pellets (central pellet on the beam axis).

We used the FLUKA Monte-Carlo transport code[6] for U-fission rates and radiation energy deposition calculations; and a 40-MeV Gaussian electron beam with 12x12-mm FWHM as a source of primary particles. We assumed that the beam axis is in coincidence with the converter axis.

FIGURE 13 represents energy deposition in the assembly's vertical section for clarity. The color scale is given in Watts per cm^3 and per 1 kW of the beam power. The central pellet, beam dump and Ta-plates in the converter absorb ~ 3.6, 18.4, and 21.5 % of the beam energy.

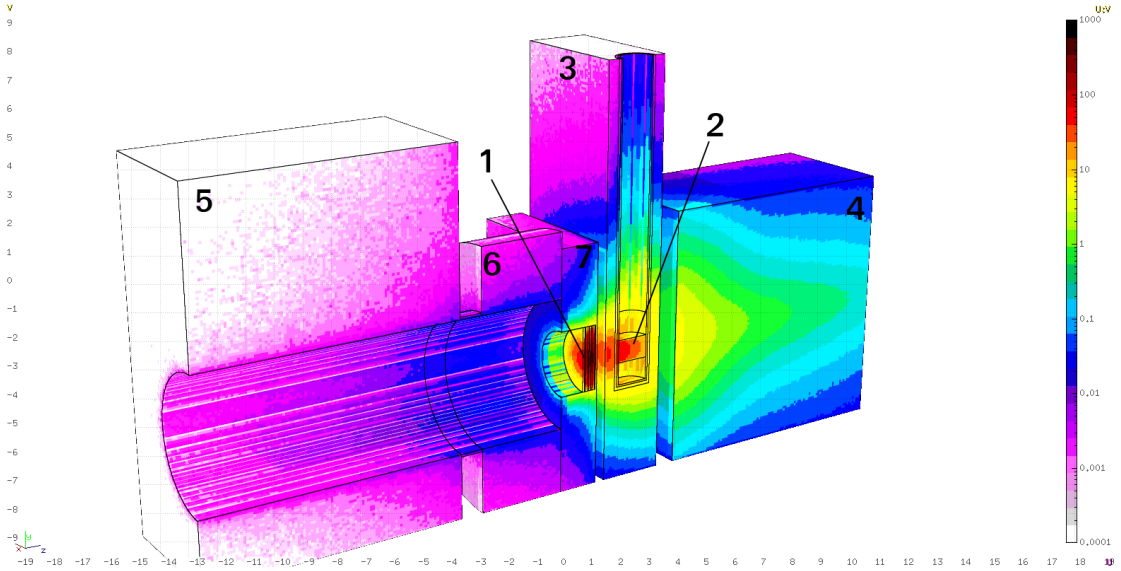

FIGURE 13 Representation of radiation energy deposition, showing: 1 = Ta converter and beam window, 2 = U_3O_8 pellet, 3 = target's container holder, 4 = beam dump, 5 = beam pipe and the assembly interconnector, 6 = flange, 7 – converter's holder

We used the Monte Carlo N-Particle (MCNP) code[7] to predict isotopes burnup in regions with fissionable material (U_3O_8 pellet). The simulations involve the use of criticality subroutine KCODE, and the burnup subroutine CINDER 90. The KCODE subroutine performs iterative calculations to calculate the effective neutron multiplication factor and Keff. We applied the burnup subroutine CINDER 90 to simulate the production of fission product isotopes and actinides in the target considering isotopes burnup and production in a neutron fields. This subroutine tracks up to 3400 isotopes.

MCNP cannot be used directly for burnup studies of subcritical systems, but it is possible to bypass this limitation by splitting the study into two steps (

TABLE 4). First, neutron spectrum and total number of fissions are calculated in the fissionable material. Second, calculated neutron spectrum and irradiation profile (beam power time-profile) are used as an external source for burnup studies and results are normalized on the total number of fissions obtained after Stage 1.

TABLE 4 Simulation Stages to Determine Isotope Production Yields

Stage 1: **(FLUKA)**	Input: Primary particles: Electron's beam Output: Radiation energy deposition. Neutrons and photons energy spectrum (in the U-pellet). Fission events collection: number of fissions; fission fragments A/Z range; fission energy.
Stage 2: **(MCNP)**	Input: Primary particles: Neutron spectrum (from stage 1). Fission power (for normalization). Irradiation beam power profile (used in BURN MCNP card). Output: Isotopes composition in U_3O_8

After the first stage, we calculated the fission reaction rates in U-pellet, and calculated photo- and neutron- induced fissions separately (TABLE 5).

TABLE 5 Fission Reaction Rates on Uranium

Isotope	Fission reaction rate (1/primary e-)	Photo fissions, % (from total number of fissions)	Neutron-induced fissions, % (from total number of fissions)
^{235}U	1.670E-6	0.87	0.18
^{238}U	1.463E-4	73.10	25.85

We performed the second stage with MCNP (KCODE and BURN studies[7]). Fission power per 1 kW beam power for 40MeV electron beam can be calculated as (1.0E+3 [W] / 4.0E+7 [eV]) * (1/qe) * RR * Ef, where *qe* is elementary charge, *RR* is fission reaction rate per primary electron and *Ef* is fission energy (typically ~ 200MeV).

In our simulations we considered four irradiation scenarios: 1.5, 3.0, 30.0, and 60.0 kW*h of total energy delivered to the Ta-converter. The 1.5-kWh, 3.0-kWh, and 30-kWh irradiations were already performed. FIGURE 14 shows real beam power profiles obtained from the Linac control system.[8] To optimize burn-up studies, we performed a reasonable averaging for each irradiation profile. For the "60kWh" irradiation scenario we assumed a constant beam power of 3 kW for 20 hours.

Activities for specific isotopes at EOB (end of bombardment) were extracted from MCNP output (burn-up data table, non-actinides inventory) and are shown in the TABLES 6 and 7. Experimental data and Activity-^{99}Mo-Activity ratios are also given for some isotopes. The agreement between gamma-measurements and simulation is decent. Activity-^{99}Mo-Activity ratios coincide within 10–15%, which indicates the correct modeling of the reaction rates. But the difference for absolute values can exceed 50% for some isotopes. As shown in Section 3.2.3, the production rates are very sensitive to the geometrical parameters of the target and its position with respect to the beam axis. Main sources of systematic errors of the simulations approach are also discussed Section 3.2.3.

TABLE 6 Activities at EOB, 1.5-kWh irradiation. Experimental activities for the first and second irradiation were determined from an aliquot of the dissolved target and uncertainties were derived from counting statistics (2σ). Values for the third irradiation were determined by averaging different stages of the chemical separation.

1.5-kWh Irradiation				
Isotope	**MCNP, Activity (µCi)**	**MCNP, Ratio: Activity/ ^{99}Mo Activity**	**Experiment, Activity (µCi)**	**Experiment, Ratio: Activity/ ^{99}Mo Activity**
^{95}Zr	16.87	0.029	21 ± 0.16%	0.024
^{99}Mo	581.7	1	873 ± 0.22%	1
^{103}Ru	38.51			
^{132}Te	387.4		415 ± 0.06%	
^{135}I	6335			
^{137}Cs	0.135			
^{140}Ba	119.3	0.205	159 ± 16%	0.182
^{144}Ce	4.285			
3-kWh Irradiation				
Isotope	**MCNP, Activity (µCi)**	**MCNP, Ratio: Activity/ ^{99}Mo Activity**	**Experiment, Activity (µCi)**	**Experiment, Ratio: Activity/ ^{99}Mo Activity**
^{89}Sr	20.68			
^{90}Sr	0.178			
^{95}Zr	35.44	0.029	33 ± 0.15%	0.042
^{99}Mo	1218	1	790 ± 1.4%	1

TABLE 6 (Cont.)

3-kWh Irradiation (Cont.)				
Isotope	**MCNP, Activity (μCi)**	**MCNP, Ratio: Activity/ ^{99}Mo Activity**	**Experiment, Activity (μCi)**	**Experiment, Ratio: Activity/ ^{99}Mo Activity**
^{103}Ru	78.96			
^{105}Ru	8189			
^{106}Ru	3.369			
^{132}Te	813.6			
^{135}I	12950			
^{137}Cs	0.284			
^{140}Ba	247.3	0.203	186 ± 0.82%	0.235
^{143}Ce	1341			
^{144}Ce	8.928			
30-kWh Irradiation				
Isotope	**MCNP, Activity (μCi)**	**MCNP, Ratio: Activity/ ^{99}Mo Activity**	**Experiment, Activity (μCi)**	**Experiment, Ratio: Activity/ ^{99}Mo Activity**
^{89}Sr	300.4			
^{90}Sr	1.821			
^{91}Y	109.6			
^{95}Zr	434.6	0.038	324 ± 51%	0.035
^{99}Mo	11350	1	9273 ± 46%	1
^{103}Ru	803.2			
^{105}Ru	51330			
^{106}Ru	32.91			
^{105}Rh	6376			
^{132}Te	7931			
^{131}I	1789			
^{135}I	79870			
^{133}Xe	947.3			
^{135}Xe	30120			
^{137}Cs	2.951			
^{140}Ba	2429	0.214	2200 ± 8.7%	0.237
^{141}Ce	470.5			
^{143}Ce	16180			
^{144}Ce	87.53			
^{143}Pr	191.5			
^{147}Nd	1189			
^{149}Pm	2745			
^{151}Pm	2888			
^{153}Sm	973.8			

TABLE 7 Activities at EOB, 60-kWh Irradiation

Isotope	MCNP, Activity (μCi)
^{85}Kr	0.3
^{89}Sr	609.2
^{90}Sr	3.65
^{91}Y	345.9
^{95}Zr	872.1
^{99}Mo	21610
^{103}Ru	1598
^{105}Ru	65890
^{106}Ru	65.48
^{105}Rh	15930
^{132}Te	15270
^{131}I	3721
^{135}I	112100
^{133}Xe	3280
^{135}Xe	68180
^{137}Cs	5.92
^{140}Ba	4792
^{140}La	742.2
^{141}Ce	1248
^{143}Ce	29890
^{144}Ce	174.2
^{143}Pr	658.7
^{147}Nd	2375
^{149}Pm	5881
^{151}Pm	5328
^{151}Sm	0.05
^{153}Sm	1841
^{155}Eu	0.79

3.2.2 Experimental Total Production

Inconsistences or high uncertainties were observed in the production determination of isotopes. The front-end solutions containing ^{237}U and the majority of FP exhibited relatively high activities compared to simulations, while those following chemical separations from the FP were slightly lower. The 208-keV photopeak from ^{237}U interfered with the prominent 181-keV ^{99}Mo photopeak and rendered it unusable, forcing us to rely on 739 keV. Still, the source of the

discrepancies are unknown, which systemically skews all downstream recovery percentages and purity levels. To explore these inconsistencies further, we analyzed a number of different samples as a function of ^{99}Mo gamma energies. The results are shown in FIGURE 14, which highlights the discrepancies.

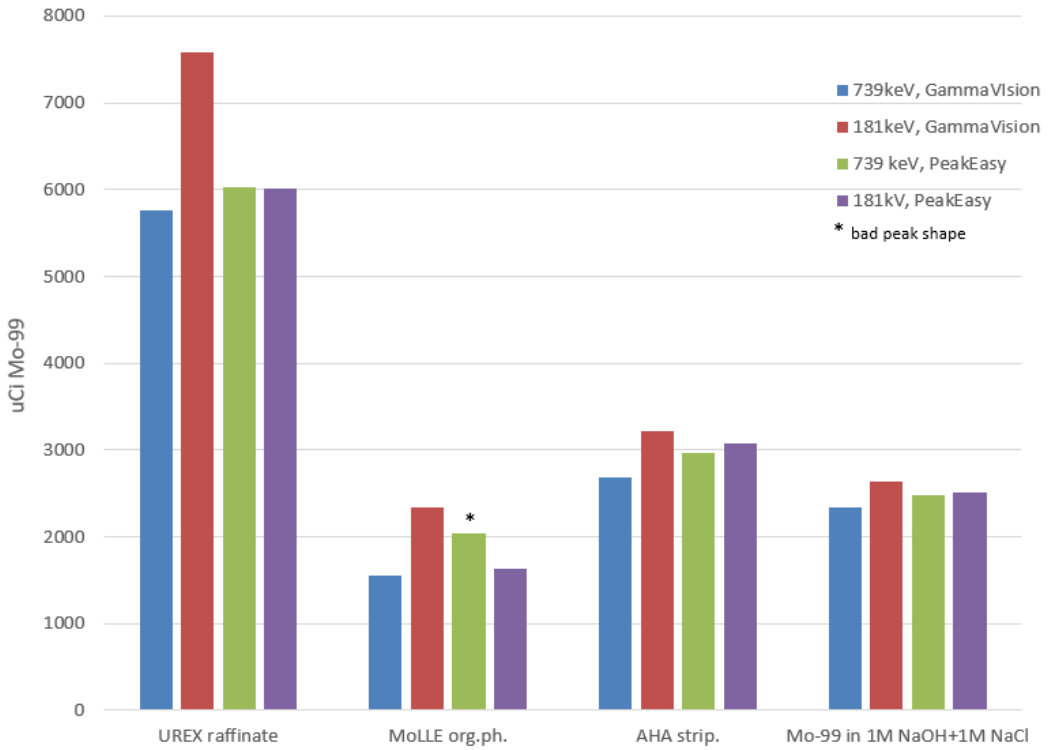

FIGURE 14 Total production of ^{99}Mo (in uCi) in various representative samples; assuming quantitative ^{99}Mo recovery, each sample should exhibit the same activity of ^{99}Mo

We analyzed UREX raffinate containing ^{99}Mo, the uranium target, and the majority of fission products in nitric acid at different distances from the detector. We treated the same data with either PeakEasy (using the detector's polynomial calibration curve) or GammaVision. Results varied at nearly every data point and a trend could not be determined (FIGURE 15).

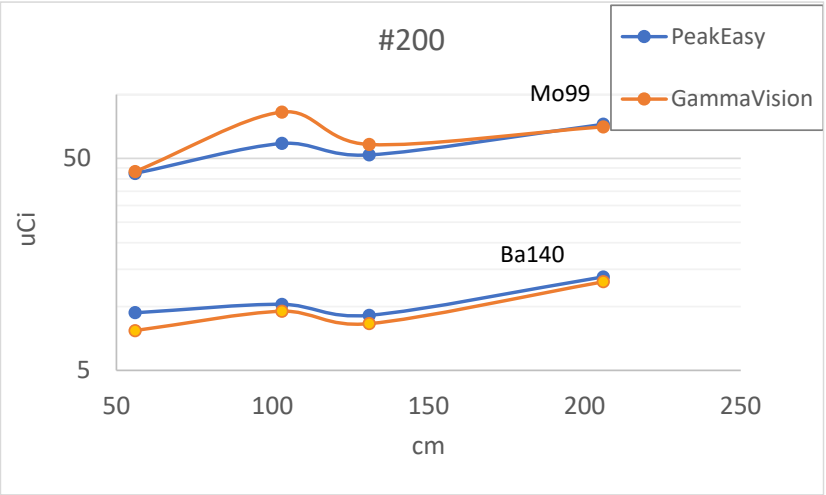

FIGURE 15 Decay-corrected activities of ^{99}Mo and ^{140}Ba as a function of distance from the detector

The same dissolved target sample was analyzed at a fixed distance from the detector at different times following EOB. Between 10–12 days after EOB, results were relatively consistent. However, after 23 days of decay, results started to vary and ^{99}Mo activities increased, while those for ^{95}Zr and ^{140}Ba decreased. Likewise, we analyzed the same sample at different distances, which also determined different yields.

3.2.3 Possible Sources of Errors

Neglecting statistical errors (<3% for all cases) we can distinguish the most important sources of systematic error in our simulations approach (isotopes calculations for the given neutron and photon spectra):
(1.) geometrical offsets (beam and pellets offsets from the axis);
(2.) photo-fission isotopic yields (assumed to be equal to neutron induced fissions); and
(3.) burn-up in photo-fields.

We performed an additional set of simulations to estimate the impact of beam and the central pellet offsets on the fission reaction rate. Deviations from the basic case — results for isotopes calculations in the central U_3O_8 pellet with zero geometrical and beam offsets — with the burn-up studies performed for neutron fields, are shown in TABLE 8. As can be seen, the system is very sensitive to the offsets, since most of fission reaction are induced by photons concentrated the cone with a small apex.

Assumption burn-up only in neutrons fields causes errors. Comparing activation integrals for nonelastic gamma reactions rates for specific isotopes gives a fist approximation of burn-up in gamma field. Corrections on “photo burn-up” were estimated for the central pellet. Data for ^{99}Mo, ^{95}Zr, and ^{140}Ba isotopes are given in TABLE 8. A simple comparison of fission yields for

neutron and gamma induced fissions also gives a first order correction for isotopes production rates in neutron and gamma fields.

As can be seen from TABLE 8, dominated sources of errors for the experimental setup are geometrical uncertainties and underestimations of isotopes burn-up in gamma fields.

TABLE 8 Systematic Error in Simulated Yields

Error Source	Deviation from the Basic Case, %	Note
Beam offset: Y = +- 4.5 mm	-26	
Beam offset: X = +- 4.0 mm	-22	
Photo-fission yields: ^{95}Zr ^{99}Mo ^{140}Ba	 +3 +3 -7	Direct comparison of fission yields for ^{238}U(n,f)[9] (for fast n-spectrum) and ^{238}U(g,f)[10] reactions
Burn-up in photo fields: ^{95}Zr ^{99}Mo ^{140}Ba	 -34 -38 -32	From a direct convolution of photo-spectrum in the sample with inelastic (g,*) cross sections[11]

3.3 NOBLE GASES AND IODINE SEPARATION CHEMISTRY

3.3.1 Noble Gases

We treated each layer of containment with an evacuated stainless steel cylinder to collect any volatiles that were released from the target. The secondary container for the target holder did not contain any active gases in all three irradiation experiments, meaning that the primary container was structurally sound and not leaking. The content of primary containment for each irradiation is shown in TABLE 9. The spectrum of the primary gas cylinder from irradiation #1 is shown on the FIGURE 16.

TABLE 9 Activity (uCi) of Gaseous Isotopes in the Primary Containment

Isotope	Irradiation #1	Irradiation #2	Irradiation #3
^{133}Xe @161 keV	10	5220	36688
^{135}Xe @250 keV	892	N/A	28164
^{85m}Kr @305 keV	0.8	-	-
^{88}Kr @196 keV	751	-	-
^{133}I @530 keV	-	4.4558	4.3932

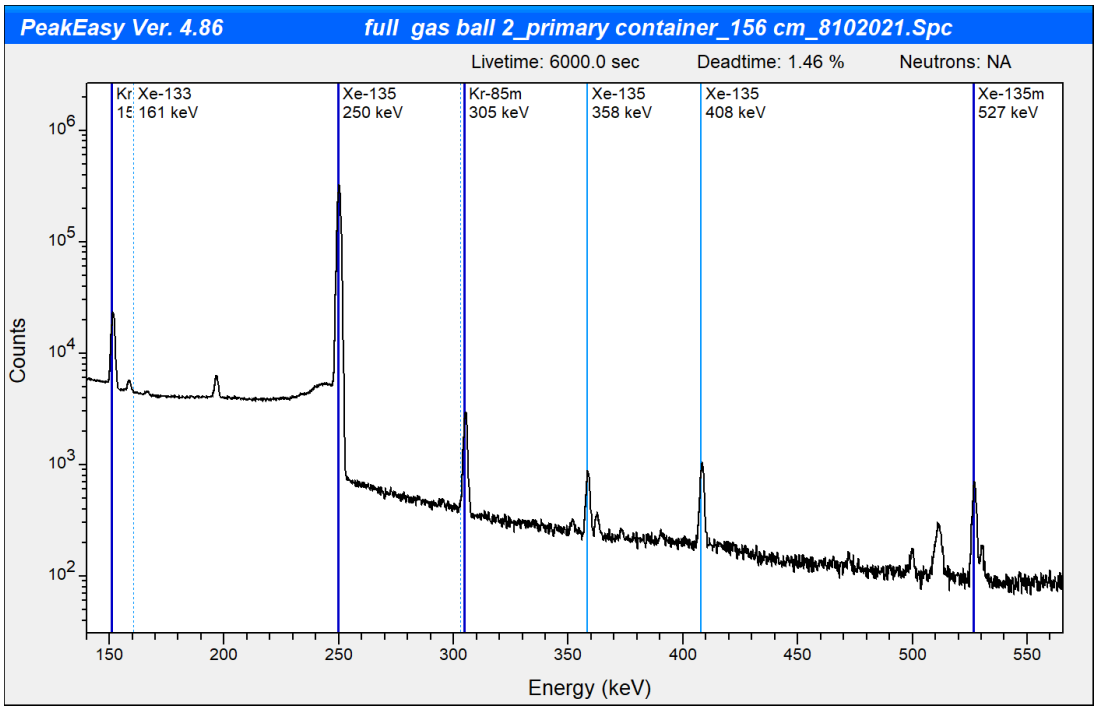

FIGURE 16 HPGe spectrum of a loaded gas cylinder from irradiation #1 containing ^{135}Xe, ^{135m}Xe, ^{133}Xe, and ^{85m}Kr

TABLE 9 lists the noble gas and iodine isotopes observed after irradiations. The activity of detected radionuclides increases with increase of dose for target. The activity of xenon isotopes progressively increased from 10 microcuries to 10,000 thousand microcuries, while the increase for the dose delivered to the target changed from 1.5 kWh to 30 kWh. The iodine became detectable in fission gases starting from irradiation #2 but its activity didn't change significantly in irradiation #3.

3.3.2 Iodine Removal

In an attempt to purify ^{99}Mo from isotopes of iodine, we tested two approaches: (1) distillation of the liquor of the dissolved target and bubbling the traps filled with NaOH and (2) bubbling over a prolonged period of time (no distillation).

In the first irradiation experiment, we evaporated the liquor of the dissolved target to dryness and condensed the vapors. The results showed that only ~10% of the ^{2}I volatilized out of the liquor. We found only a small fraction of the I_2 in the distillate and the NaOH trap (FIGURE 17). Ru was volatile and a significant quantity was found in the distillate. The dodecane trap, although not useful for capturing I_2 or Ru, also serves as a safety to prevent gas release into the hood — consequently, we recommend leaving it in place.

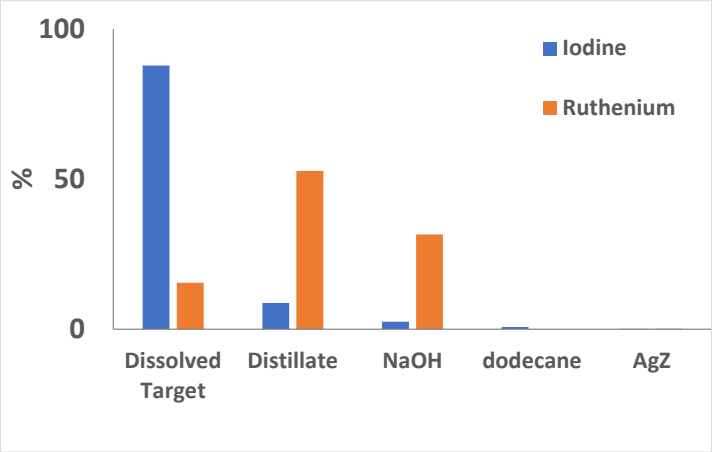

FIGURE 17 Capturing iodine and ruthenium in irradiation experiment #1

For the second and third irradiations, we did not distill the liquor of the dissolved target but instead explored the efficiency of iodine capture by NaOH traps as a function of time of bubbling the liquor. In this context, the principal difference between the second and third irradiations was the variation of temperature and power of bubbling within the experiment for irradiation #2. The initial content of traps was the same for irradiations #2 and #3: two traps with 1M NaOH, Drierite trap, AgZ trap.

FIGURE 18 shows, for the second irradiation, the results of the timed experiment on iodine capture by bubbling. With the only outlier at 172 minutes, the scatter plot for trap #1 (top, FIGURE 18) shows a strong, positive, linear association between time of bubbling the solution in traps and total activity of iodine radioisotopes in traps. The points at 172 minutes and 231 minutes correspond to temperature increases and decreases of pressure in the system, respectively. Short-term temperature increases caused a spike of activity, but the effect diminished as the temperature fell after 172 minutes.

The decrease in the total activity of radioiodine can be explained by a conversion of iodine to molecular iodine that escapes the trap. Starting from 231 minutes, the excess bubbling occurred but the rate of activity increase didn't change significantly compared to the range 0-142 mins. As expected, the second trap (bottom, FIGURE 18) has lower iodine activity but it is still not negligible, justifying its use for the purpose of complete iodine capture. The rate of radioiodine accumulation in the trap #2 is strongly positive, but its linearity is blurred mostly because of the dominant contribution from trap #1 and lower activities.

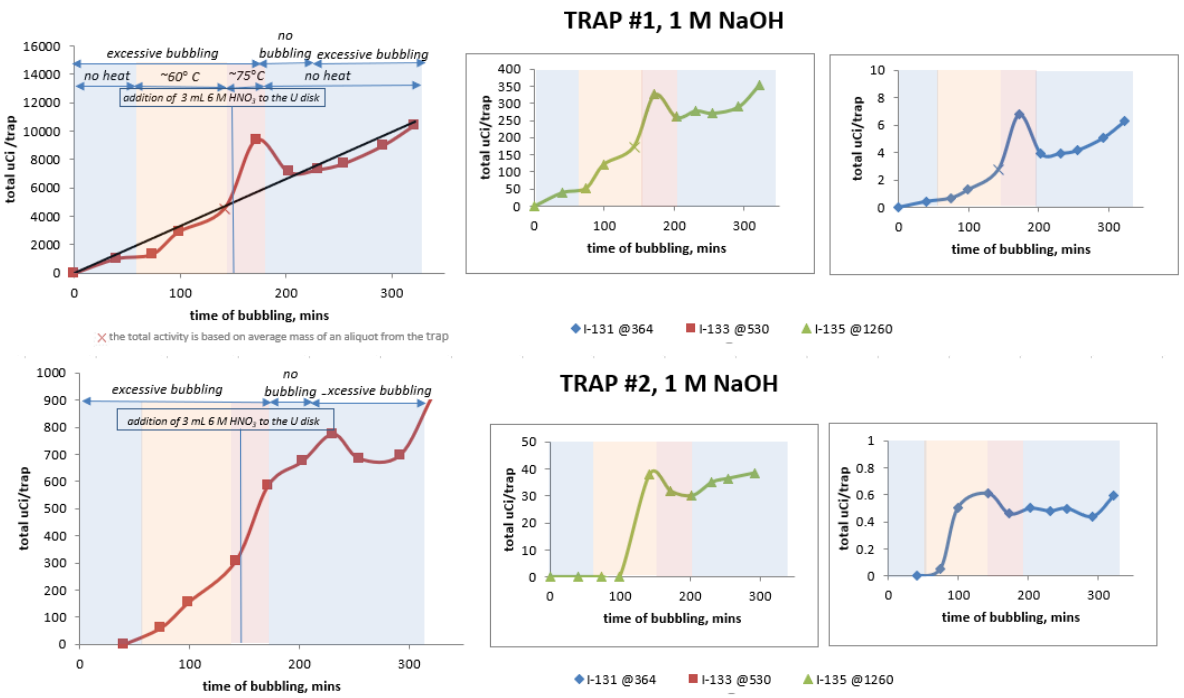

FIGURE 18 Iodine capture by bubbling for irradiation #2 — Trap #1 (top), Trap #2 (bottom)

For the third irradiation, after the target dissolved, we bubbled the system through two NaOH traps for ~3 hours by applying a constant slightly negative pressure, keeping the temperature at ~60°C. As with irradiation #2, we observed a linear increase of radioiodine over time in both traps. Approximately 14% of total ^{131}I content and 33% of ^{133}I was captured by two traps (FIGURE 19). Since these values should not depend on the isotope, the difference likely stems from the uncertainties in total production of iodine (see Section 3.2 Total Production of Isotopes: Monte-Carlo Simulations). However, the slopes shown in FIGURE 19 are nearly identical. Slow evolution of iodine into solution upon bubbling might be indicative of slow transformation of speciation, i.e., conversion of I_2 to I^-.

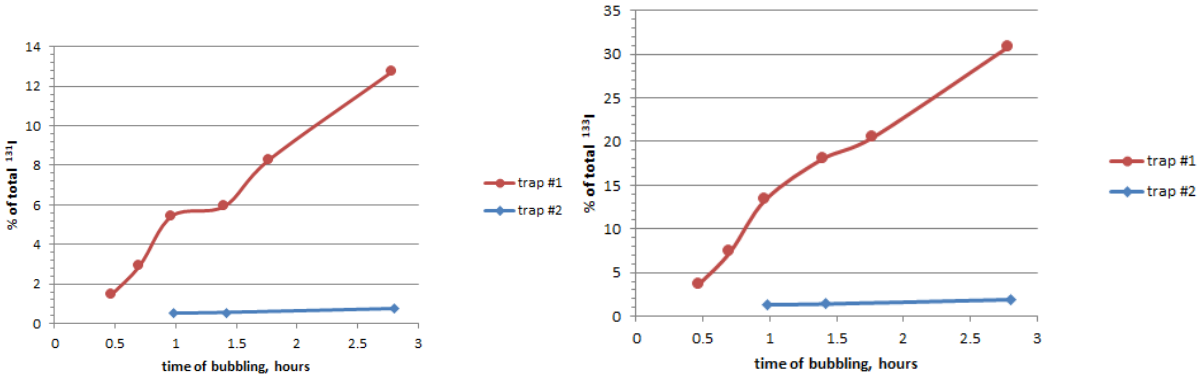

FIGURE 19 Iodine capture by bubbling for irradiation #3 — Trap #1 (left), Trap #2 (right)

The option of bubbling the uranyl nitrate solution for iodine removal did not provide satisfactory results. The evolution of iodine by bubbling was very slow and isn't a practical solution due to losses of ^{99}Mo, where about 1% of ^{99}Mo is lost each hour. The solvent and column elution should be explored in more details to purify the ^{99}Mo product from the radioiodine.

3.3.3 Iodine Speciation

To better understand iodine behavior, we investigated iodine speciation in uranyl nitrate solution after irradiations #2 and #3. After the second irradiation, the composition of iodine species was as follows: (FIGURE 20): 45% molecular iodine; 15% iodide; 40% iodate/periodate.

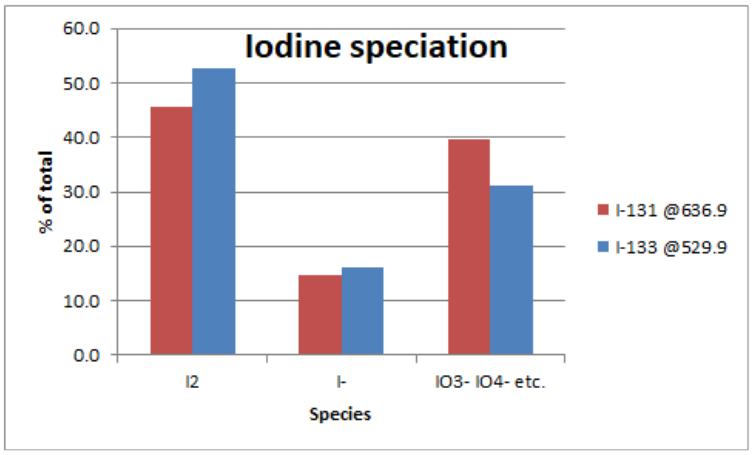

FIGURE 20 Iodine speciation for dissolved target for irradiation #2

For irradiation #3, the speciation of ^{131}I in the initial uranyl nitrate solution is the following (FIGURE 21): 15% molecular iodine; 35% iodide; 50% iodate, periodate, etc. Contrary to the previous irradiation (3kWh), the percentage of molecular iodine decreased by 30% and the difference was distributed between iodide and periodate nearly proportionally.

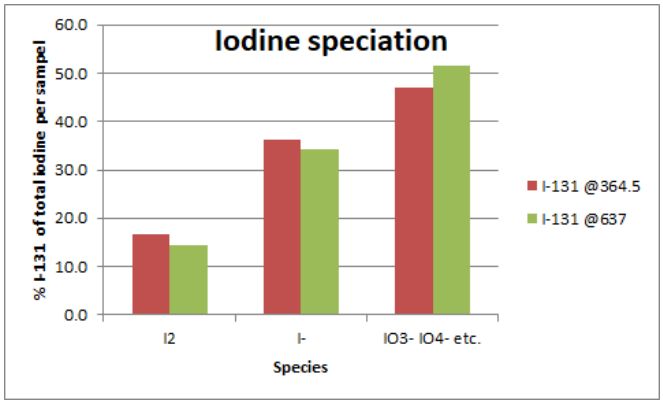

FIGURE 21 Iodine speciation for dissolved target for irradiation #3

Based on the results of the iodine speciation for these two irradiations, we can state that the iodine speciation changes with burnup, time, and the use of air to bubble the target solution. Based on these data, it is expected that for longer irradiations, the fraction of molecular iodine would decrease, while the fraction of iodate and periodate would increase. This speciation is very relevant in the context of ^{99}Mo processing, since ^{131}I has been observed in every stage of UREX, MoLLE, and the concentration column. Furthermore, ^{131}I has a very low tolerance in QA/QC fission product limits. It is believed that elemental I_2 is the primary species that fractionates into the organic solvents. We are exploring several options to better manage iodine in this system to include initial redox adjustments to promote unextractable iodide or leveraging anion exchange column chemistry to remove iodine during the acidic wash steps.

3.4 TARGET DISSOLUTION

3.4.1 Target Dissolution — Irradiation #1

We treated the pellet from Irradiation #1 using the setup shown in FIGURE 22 and FIGURE 23. We dissolved the pellet in 20 mL of 6M HNO_3 and boiled it to dryness with a heating mantle. We added the extra volume to ensure complete dissolution since the target was going to be evaporated to dryness. The distillate was then condensed into a 50-mL round-bottom flask using a chilled water bath flowing through a condensing coil. The evaporation took approximately 3 hours to achieve dryness. Afterwards, we observed a dark-orange uranyl salt at the bottom of the dissolution vessel. The system was held under slight negative pressure and the gases were fed through 50 mL of 1M NaOH, 45 mL of dodecane, a Drierite trap, and a Drierite + AgZ trap.

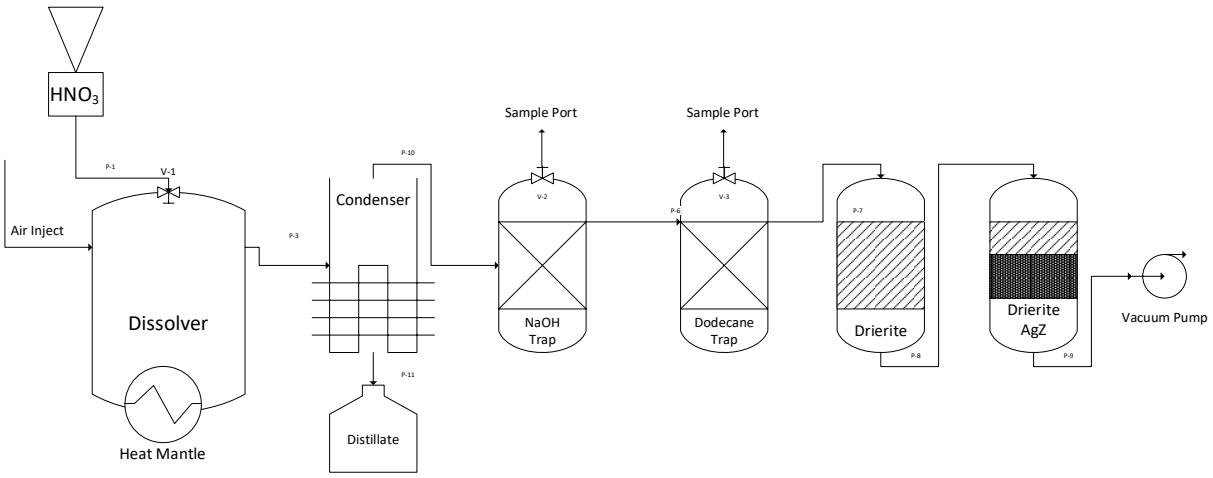

FIGURE 22 Dissolution setup for irradiation #1

FIGURE 23 Setup for chemical processing after irradiation #1

3.4.2 Target Dissolution — Irradiation #2

The dissolution schematic is illustrated in FIGURE 24. We removed the condenser used after irradiation #1 (FIGURE 22). Since evaporation of the uranyl target solution did not remove a significant amount of iodine (FIGURE 17) and the operation was time-consuming, we eliminated this step. We then made the decision to evolve iodine from the target solution using air-sparging into the NaOH traps, and replaced the dodecane trap with another NaOH trap in order to improve iodine collection.

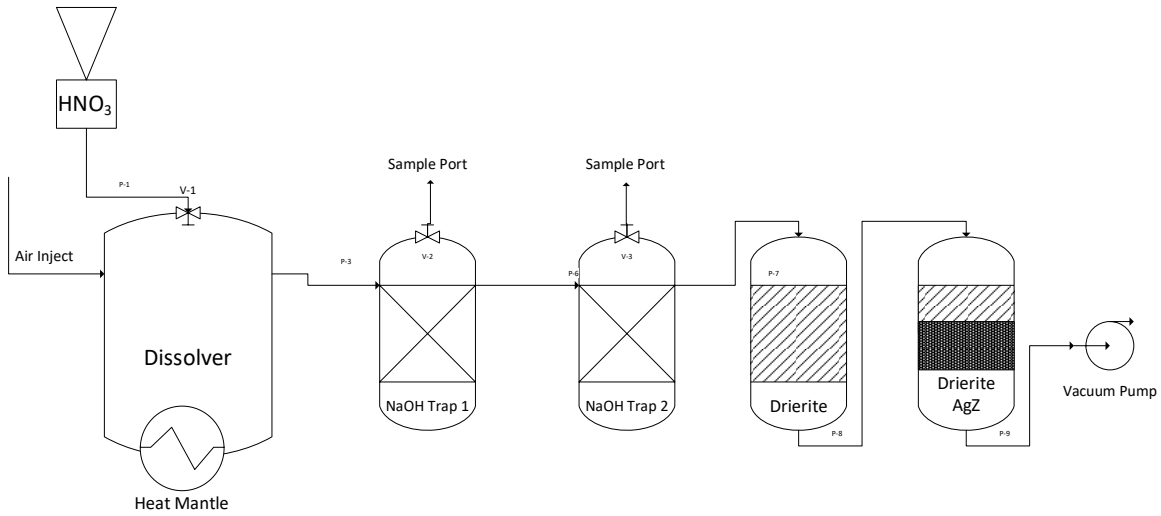

FIGURE 24 Dissolution schematic for irradiations #2 and #3

We added a volume of 17.5 mL of 6M HNO_3 to the dissolver with rigorous air bubbling during the dissolution. The overall operation took longer than expected and was inefficient. During the dissolution, we increased the volume of acid to 20.5 mL of 6M HNO_3. The temperature was first increased to 65°C and then to 77°C all while continuing rigorous air bubbling. After several hours, the U target was not fully dissolved. We ceased the air bubbling and dissolution proceeded much quicker until we observed the bright yellow solution. These observations reflect previous results of Inoue et al., who noted that U_3O_8 dissolution rates are strongly associated with agitation and stirring speed.[12] The rigorous air bubbling evolved NO_x gases (and subsequently lowered surface NO_2^- concentrations), which act as a catalyst for U_3O_8 dissolution. As a result, the overall dissolution took several hours and was incomplete based on residual solids. During the entire operation, samples were withdrawn from both NaOH traps (~0.2–0.3 mL of each) and counted.

We removed the uranyl solution from the dissolution vessel and withdrew two representative 7 mL samples, then performed an H_2O rinse of the dissolution flask to remove some undissolved solids (derived from either incomplete dissolution described above or small amounts of UO_2 impurities) and residual uranyl solution.

3.4.3 Target Dissolution — Irradiation #3

We dissolved the target in 17 mL of 6M HNO_3 without air-bubbling and under a slight vacuum at 77°C. The dissolution setup comprised the vessel, two 1M NaOH traps, a Drierite trap, and an AgZ trap (the same setup shown in FIGURE 24). The dissolution took approximately 20 minutes, which was a substantial improvement over irradiation #2. After the pellet dissolved completely, we turned off the heat and began rigorous bubbling through the uranyl solution in order to evolve and trap iodine from the target solution. The results of the iodine evolution are discussed above and plotted in FIGURE 19.

3.5 ^{99}MO PURIFICATION

The approach to purifying the ^{99}Mo from the dissolved uranium target was generally the same across all three irradiations. We used three contacts of 30% TBP to remove the uranium. Three contacts with 0.4M HDEHP removed the ^{99}Mo and three contacts of 0.5M AHA (pH 1) stripped the ^{99}Mo along with trace quantities of Nb, Np, I, Zr, and Te. The O:A are described below. For the third irradiation, we added an HNO_3 scrub in between the loading step and the AHA strip to improve fission product removal. We also treated the concentration column using the same using 20 mL of eluent with NaOH to remove Zr, Np, and Te; 40 mL of HCl + oxalic acid to remove Nb; 10 mL of HCl to remove oxalic acid; and 15 mL of NaOH + NaCl to recover the ^{99}Mo. Slight iterations in concentrations and their effects are discussed below.

3.5.1 ^{99}Mo Purification — Irradiation #1

We dissolved the dried uranyl salt ($UO_2(NO_3)_2$-hydrate) in 16 mL of 3M HNO_3. The solution was then split (1: ~8 mL, 2: ~11 mL with an H_2O rinse to remove solution) into two batches for further processing. The first batch was extracted with ~4:1.5 O:A 30% TBP twice. The third contact contained roughly 1:1 O:A TBP to remove any residual uranium.
The raffinate, containing ^{99}Mo, was brought into contact with 0.4M HDEHP (dodecane) at ~1:2 O:A two times to extract ^{99}Mo and other tracers. We used a third contact of approximately 1:6 O:A 0.4M HDEHP to clean the interface. The loaded HDEHP, containing ^{99}Mo was then brought into contact with 0.5M AHA (0.1 M HNO_3) at 1:1 O:A three times to strip ^{99}Mo. We detected a ~2% ^{99}Mo loss during these extraction steps.

We combined the AHA strips and adjusted the pH with 1 mL of concentrated NH_4OH to basic conditions. The first batch was fed through 1-g of AG-MP-1 by gravity. We rinsed the vial containing the AHA strip with 1M NaOH and fed it through the column. A significant (~30%) amount of ^{99}Mo eluted through the column during this stage. It is possible that 1M NaOH is too alkaline for this step and competes for anion sites with molybdate. These results are unusual because 1M NaOH has exhibited some success in the past especially when decontaminating ^{132}Te. During the alkali wash step, the majority of the trace ^{95}Zr, ^{239}Np were removed. Traces of iodine and ^{95}Nb were also detected, but not entirely eluted. We then washed the column with 5M HCl + 0.2M oxalic acid to remove ^{95}Nb; 5M HCl to remove oxalic acid and traces of iodine; then 1M NaOH + 1M NaCl to strip ^{99}Mo. Results showed good decontamination from the remaining fission fragments: Te, I, Np, Zr, Nb as plotted in FIGURE 25. However, the 30% loss was unacceptable and the second attempt approached the same column with lower alkalinity.

We processed the second batch in a similar manner to the first, via TBP then HDEHP extraction, with changes made to the column eluates. Rather than using 1M NaOH to rinse the vials, we used 0.01M NaOH. The results showed 2.6% ^{99}Mo loss during this step, which supports the notion that 1M NaOH was likely too concentrated. However, we observed fewer fission products in this wash step compared to the first batch (FIGURE 25). We then treated the column in the same manner as described above: 5M HCl + 0.2M oxalic acid to remove Nb, and HCl to remove oxalic acid and traces of iodine. The 1M NaOH + 1M NaCl wash contained nearly all of the ^{99}Mo, but some trace amounts of FP were observed after 15 mL: ^{132}I (daughter

of ^{132}Te), ^{131}I (0.6%), and ^{132}Te (1.8%). We estimate the ^{99}Mo recovery percentage to be 92 ± 4% based on the 739 keV gamma lines of ^{99}Mo.

3.5.2 ^{99}Mo Purification — Irradiation #2

The dissolved target was split into two 7-mL batches and was processed to recover ^{99}Mo. For UREX, the solution was treated the same as described in irradiation #1: two contacts of ~4:1.5 O:A 30% TBP; the third contact contained roughly 1:1 O:A to remove residual uranium. The second extraction stage (MoLLE) was also treated the same consisting of two ~1:2 O:A contacts of 0.4M HDEHP and a third contact of ~1:6 O:A to clean the interface. Then, we brought the combined HDEHP phases, containing ^{99}Mo and trace amounts of fission products, into contact three times with a 1:1 O:A solution of 0.5M AHA (pH 1). The distribution of notable fission products across each extraction step is plotted in FIGURE 26.

The pH of AHA strip solution was then adjusted by adding 1 mL of concentrated NH_4OH and fed through the concentration column (1g AG-MP-1) that was preequilibrated with 0.01M NaOH. The column steps comprised 15 mL 0.01M NaOH wash to lock in molybdate and remove AHA, 15 mL 1M NaOH to remove Zr and Np, 40 mL 5M HCl + 0.2M oxalic acid to remove Nb, 10 mL 5M HCl, followed by 15 mL 1M NaOH + 1M NaCl as the ^{99}Mo product. The relative percent recovery elution profiles are shown in FIGURE 27. Some Te was observed (10 nCi, 16%) after ~12 mL of 1M NaOH + 1M NaCl. The overall ^{99}Mo recovery was determined to be >100%; this error is also likely correlated to the production section described above (See Section 3.2 Total Production of Isotopes: Monte-Carlo Simulations). No fission products other than ^{99}Mo were observed in the 1st 5 mL fraction of the 1M NaOH + 1M NaCl wash which contained 92% of the ^{99}Mo product.

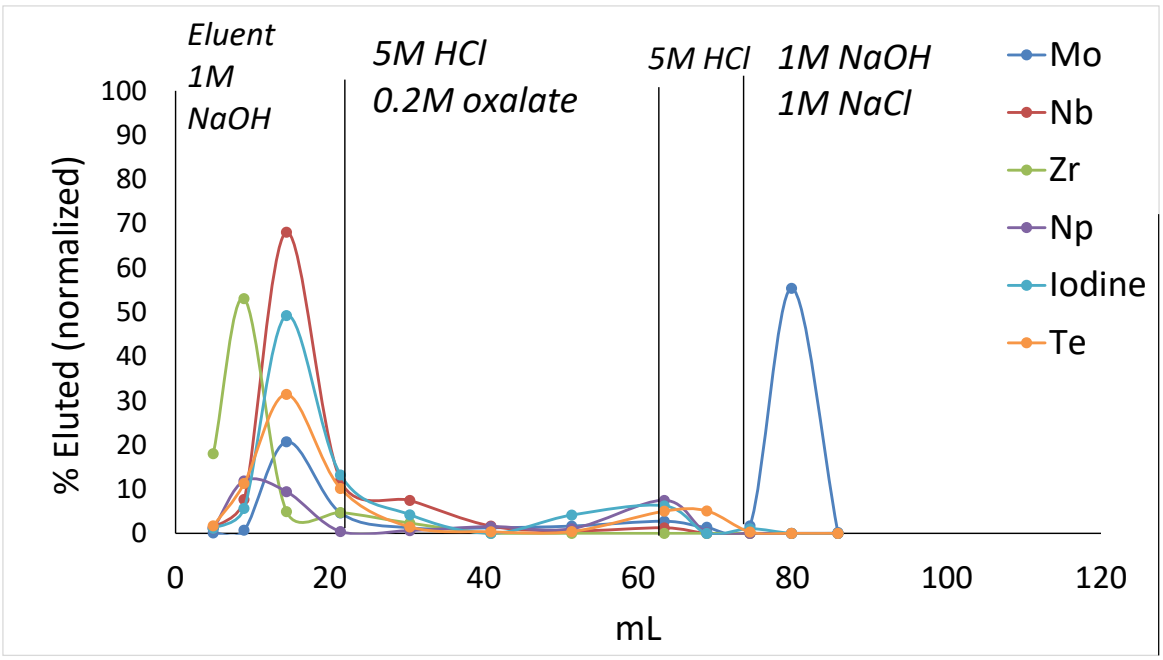

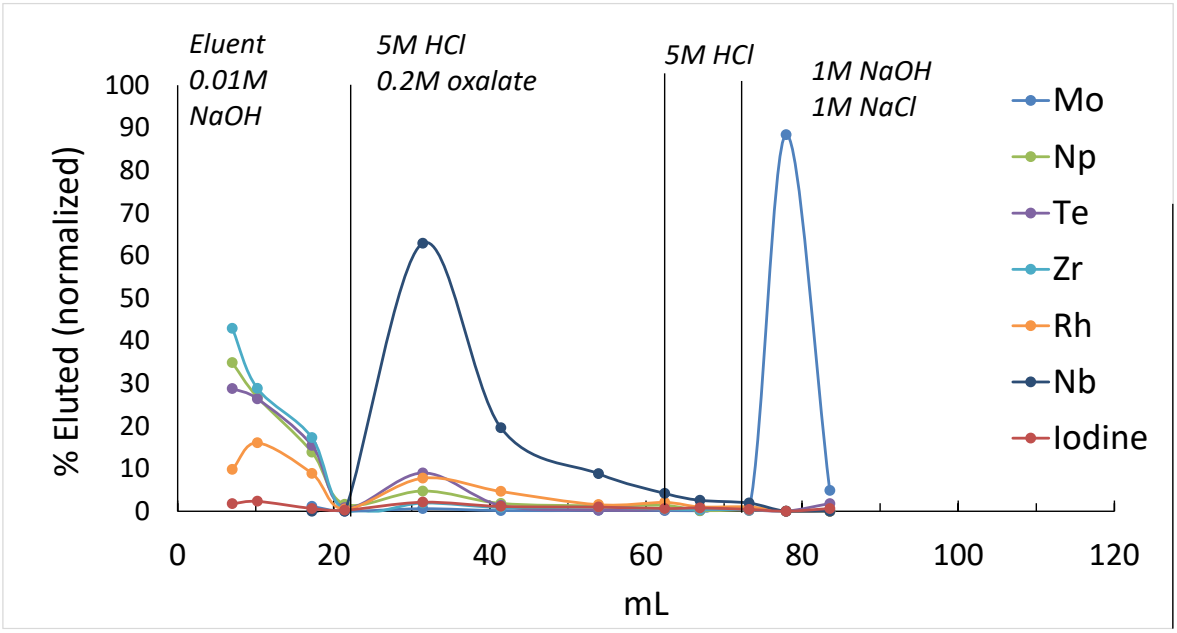

FIGURE 25 Concentration column elution profile for irradiation #1 (top) batch #1 and (bottom) batch #2

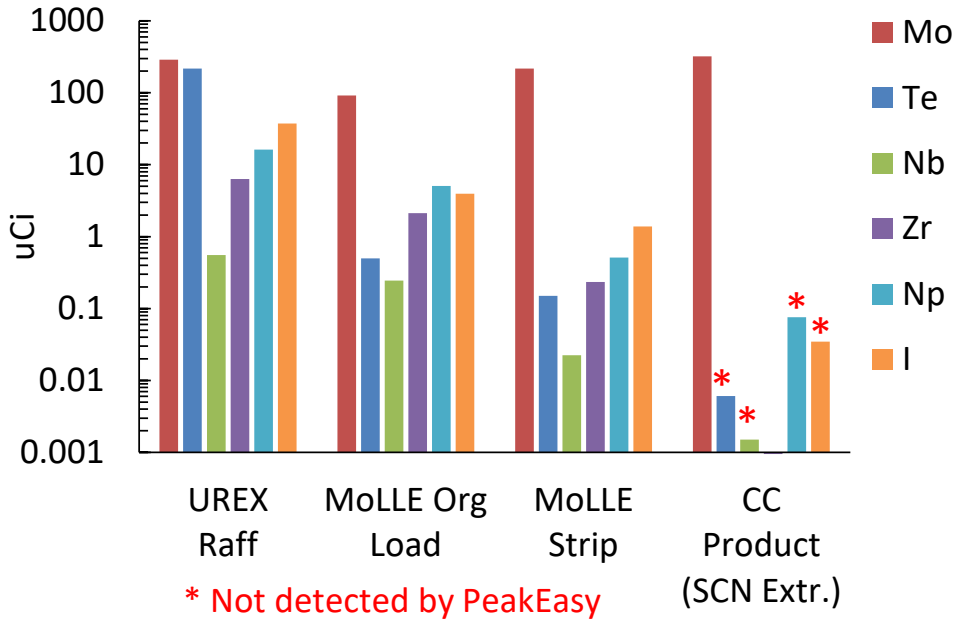

FIGURE 26 Activity profile of ^{99}Mo and selected isotopes in each stage of purification in irradiation #2

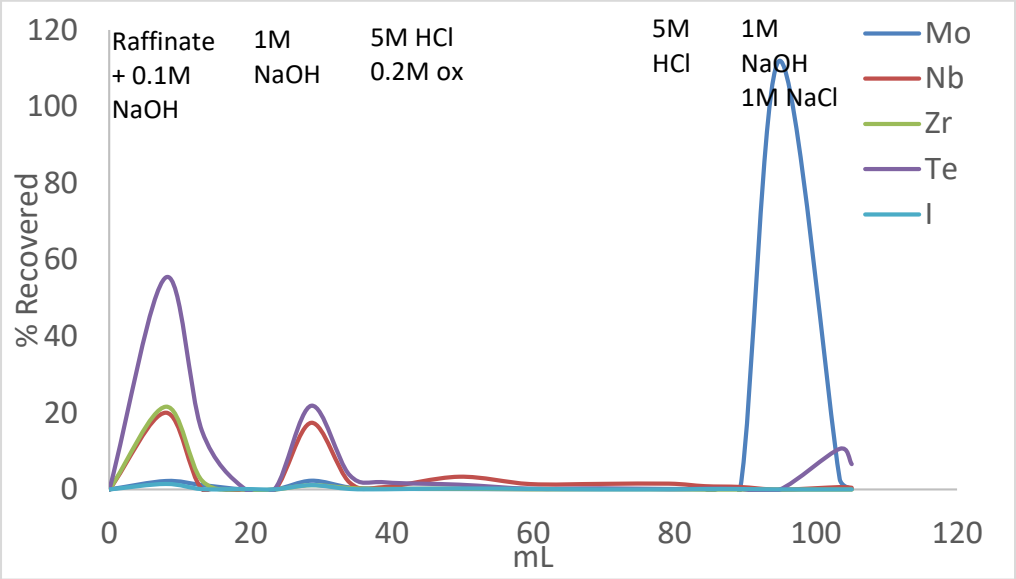

FIGURE 27 Concentration column elution profile for irradiation #2 showing relative activities of ^{99}Mo and selected isotopes

3.5.3 ^{99}Mo Purification — Irradiation #3

We fractionated the dissolved target (~16 mL) into two sections. The first (7.5 mL) was processed by the same extraction and anion exchange methods outlined above with an updated scrub section in MoLLE. The purpose of this scrub was to assess if Np, Te, Zr, Nb, or iodine could be removed, since these isotopes can require significant volumes of acid to decontaminate from the anion exchange concentration column. After the UREX and the MoLLE loading step, we brought the loaded HDEHP into contact with~1:2 O:A of 3M HNO_3; the results are shown in FIGURE 28. Although the scrub improved fission product decontamination, there was a ~2% ^{99}Mo loss during this step, which suggests the need for careful evaluation if implementing this type of scrub to remove impurities. We then brought the loaded HDEHP into contact with 0.5M AHA (pH 1) in the same ratios as described in irradiations #2 and #3 to strip the Mo along with trace amounts of I, Te, Np, Zr, and Nb.

The UREX extractions performed as expected: only trace ^{237}U was detectable in the UREX raffinate indicating good uranium removal. We transferred approximately 2% of ^{99}Mo into the TBP organic phase (bad peak shape was reported, however) along with trace quantities of ^{95}Zr, ^{131}I, ^{140}Ba, and ^{103}Ru. The MoLLE extraction removed all the of the ^{99}Mo to the extent that no ^{99}Mo was detected in the aqueous phase. The AHA strip, while having removed the majority of the ^{99}Mo activity, left approximately 10% (~300 uCi) of ^{99}Mo in the HDEHP. These results are unusual, since the D value is approximately 0.1 and three contacts were able to quantitatively remove ^{99}Mo in the previous trials. It is possible that the AHA solution (pH 1 HNO_3) may have degraded and decreased in concentration owing to the hydrolysis of AHA[13] since it was prepared nearly three months prior. The recommendation forward will be to prepare fresh solutions for each batch.

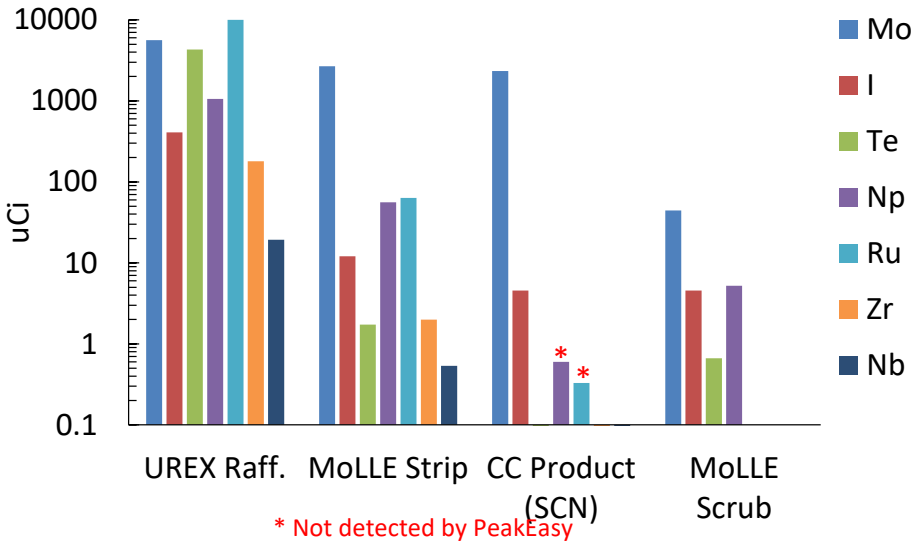

FIGURE 28 Activity profile of ^{99}Mo and selected isotopes in each stage of purification in irradiation #3

The column contained 1.5 g of AG-MP-1 that was preequilibrated with 0.01M NaOH. The elution profiles are plotted in FIGURE 29. We neutralized the MoLLE strip (0.5M AHA) with 1 mL of concentrated NH_4OH, and then washed the feed ed with 0.01M NaOH followed by 1M NaOH. The increase in alkalinity enhanced the removal of Te, iodine, and Ru with the consistent Mo loss of about 9–10%. Most of the ^{99}Mo loss occurs during the feed. It may be possible that too much NH_4OH increased the pH to >14, where the Kd of Mo has been reported to be relatively low (<100 mL/g). Future work will focus on adjusting the pH of the MoLLE strip to approximately 10–11. The HCl + oxalate and HCl wash steps are also contributing to a ~4–5% ^{99}Mo loss. We will investigate if lowering the HCl concentration in both eluates to 4M will improve this separation. We did observe a significant amount of iodine during the HCl wash steps; the high percent losses may be correlated to the high uncertainties in production yields (see Section 3.2).

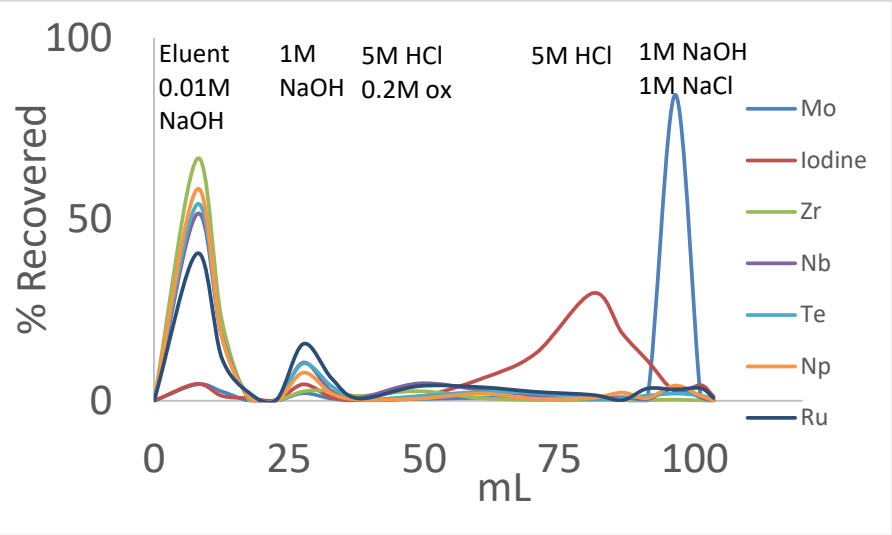

FIGURE 29 Concentration column elution profile for irradiation #3 showing relative activities of ^{99}Mo and selected isotopes

3.6 ^{99}MO PRODUCT PURITY

To determine presence of FP in ^{99}Mo product, we used two solvent extraction methods. Thiocyanate extraction selectively removes Mo and allows detection of other FP like Ru, Rh, and others. To detect activity of iodine, we performed selective iodine extraction, followed by QA/QC control for ^{99}Mo product of irradiations #2 and #3.

3.6.1 Thiocyanate Extraction (QC Procedure)

The results of thiocyanate extraction indicate that the ^{99}Mo products for irradiation #2 (FIGURE 30) and irradiation #3 (FIGURE 31) contain no radiocontaminants (^{103}Ru, ^{106}Ru, ^{125}Sb, etc.).

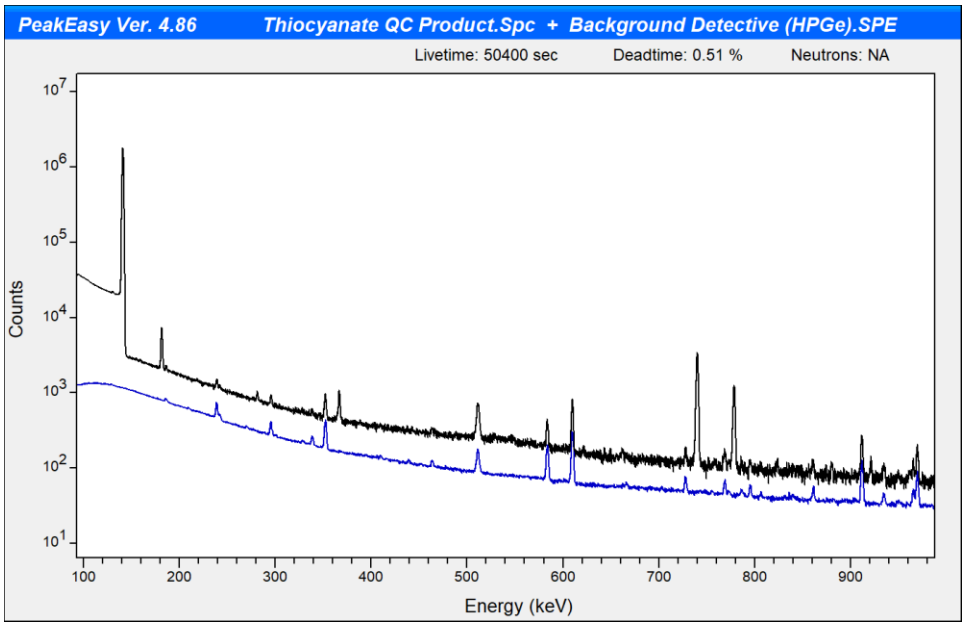

FIGURE 30 The spectrum of the product of irradiation #2 after the thiocyanate extraction compared to the background spectrum (bottom)

Comparison of the post-extraction product with a background spectrum confirms that the spectra of both products after thiocyanate extraction contain no other peaks, but ^{99}Mo peaks at 366 keV, 740 keV, 961 keV, and background peak of ^{208}Tl, ^{214}Bi, and ^{40}K.

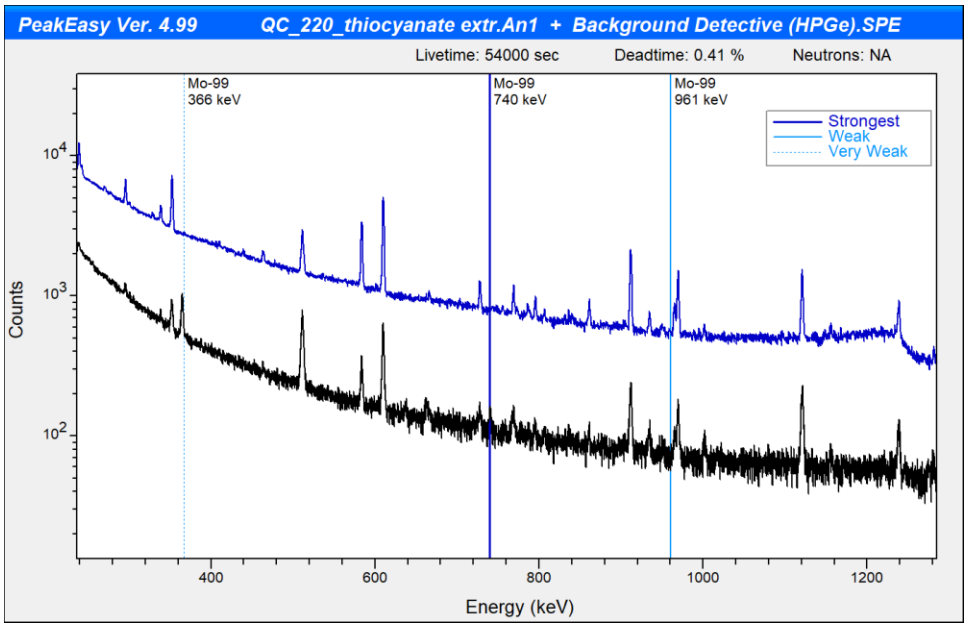

FIGURE 31 The spectrum of the product of irradiation #3 after the thiocyanate extraction compared to the background spectrum (top)

Even though the ^{99}Mo peaks are still present after the thiocyanate extraction due to incomplete ^{99}Mo extraction, the significantly lower activity of ^{99}Mo and the count time of 8+ hours for the post-extraction samples allows us to safely conclude that there are no radiocontaminants of interest in the product or their activity falls under the detection limit. Therefore, the eluate product fulfills the criteria for the nuclear-medical application.

3.6.2 Extraction of Iodine Impurities (QC Procedure)

The nuclear medicine requirement for radioiodine impurity in ^{99}Mo product requires a separate quality control procedure to detect the limit of 0.05 uCi/uCi ^{99}Mo. The ^{99}Mo eluate products from irradiations #2 and #3 were a subject of selective iodine extraction.
The spectrum of the product for irradiation #2 after iodine extraction posed no peaks of ^{131}I, indicating the highest purity of the product with regards to radioiodine isotopes (FIGURE 32).

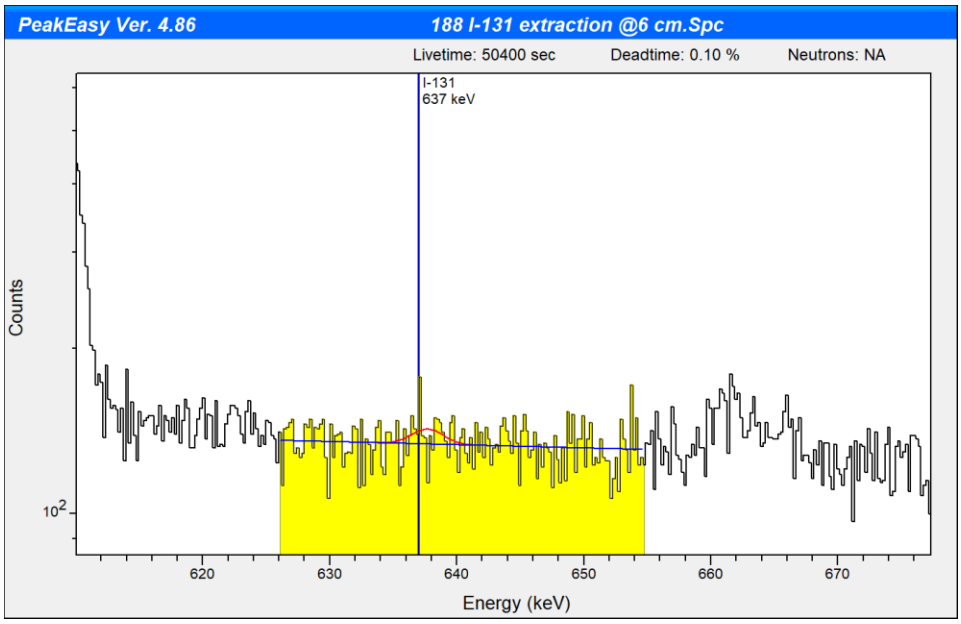

FIGURE 32 The spectrum of the product of irradiation #2 after the iodine extraction

We detected some ^{131}I in the product of irradiation #3 (FIGURE 33). However, its activity of 0.035 uCi/1 mCi ^{99}Mo falls below the minimum required limit for ^{99}Mo nuclear-medicine applications (0.05 uCi/uCi ^{99}Mo). There is a high uncertainty of the activity of ^{131}I in the sample because of the badpeak shape (FIGURE 33).

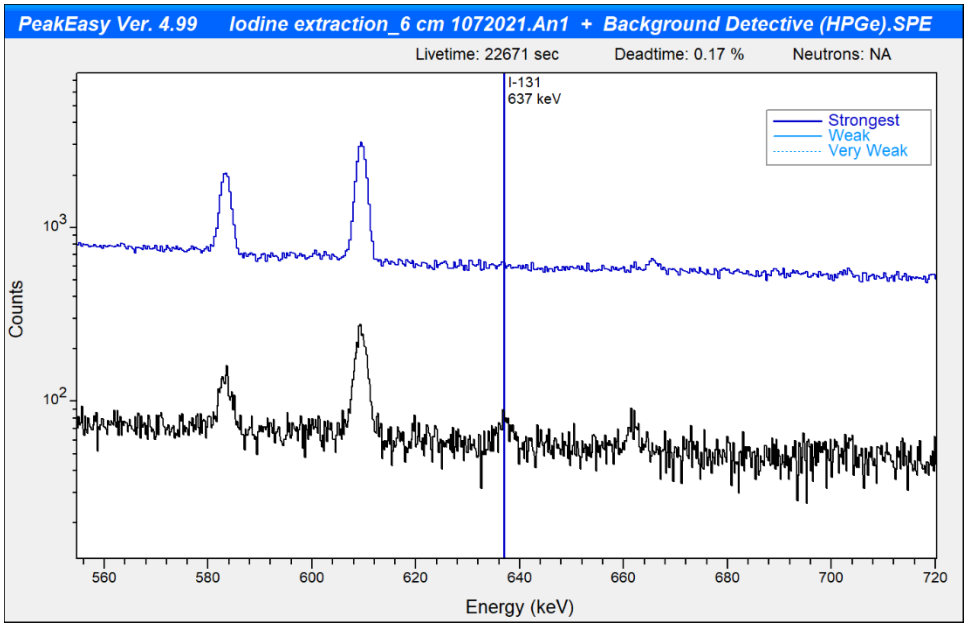

FIGURE 33 The spectrum of the product of irradiation #3 after the iodine extraction compared to the background spectrum (top)

To adress the potential issues with radioiodine impurities, we plan to introduce the step of additional column elution by HCl + oxalate in future runs, where irradiations will allow us to generate more iodine in the target.

4 CONCLUSIONS

Three irradiations of U_3O_8 pellet with total power of 1.6, 3.0, and 30 kW-hr were performed at Argonne National Laboratory's Low-Energy Accelerator Facility (LEAF) with good target containment observed during all three irradiations. As expected, we detected the presence of Xe and Kr isotopes in the primary containment of the target assembly. This is due to low packing density of U_3O_8 pellet that allows us to capture Xe and Kr. After the second (3-kWh) and third (30-kWh) irradiations, we detected the presence of iodine in the primary containment.

The dissolution of U_3O_8 in HNO_3 is optimal with high temperatures and no agitation, which can disturb NO_x surface reactions. Approximately 20 minutes are required to completely dissolve one 5-g U pellet without agitation or air-sparging. An acid concentration of 6M and 17 mL was sufficient for one U_3O_8 pellet to yield a final HNO_3 concentration of approximately 2.7M. Removal of radioiodine from the dissolved pellets by air-sparging was proven to be ineffective, with a rate of approximately ~5%/hr. We are investigating more efficient methods of removing radioiodine prior to chemical processing to recover ^{99}Mo.

The combination of UREX and MoLLE extraction processes proved to be effective for removing bulk uranium and purification of ^{99}Mo. Acetohydroxamic acid can effectively remove ^{99}Mo from the HDEHP in MoLLE process. In combination with anion exchange column, ^{99}Mo can be purified from fission products and recovered in sodium hydroxide. Careful control of the pH is needed to ensure full ^{99}Mo capture during the initial feed; excess OH^- can compete with molybdate and result in losses. The HCl steps contribute to relatively small ^{99}Mo losses and could potentially be leveraged to remove ^{131}I. More work is needed in scaling this column to accommodate multiple batches and higher volumes.

5 REFERENCES

1. V.N. Starovoitova, L. Tchelidze, and D.P. Wells, "Production of medical radioisotopes with linear accelerators," *Appl Radiat Isot* **85**, 39–44 (2014).

2. S. Mirzadeh, L.F. Mausner, and M.A. Garland, "Reactor-Produced Medical Radionuclides," in *Radiochemistry and Radiopharmaceutical Chemistry in Life Sciences*, A. Vertes, S. Nagy, Z. Klencsar, and F. Rosch, Eds. Kluwer Academic Publishers: The Netherlands, Vol. 4, p. 33 (2003).

3. M.A. Brown et al., "Recovery of high specific activity molybdenum-99 from accelerator-induced fission on low-enriched uranium for technetium-99m generators," *Sci Rep* **11**(1), 13292 (2021).

4. A.V. Gelis et al., "Closing the Nuclear Fuel Cycle with a Simplified Minor Actinide Lanthanide Separation Process (ALSEP) and Additive Manufacturing," *Sci Rep* **9**(1), 12842 (2019).

5. K. Sanyal et al., "Direct Determination of Oxidation States of Uranium in Mixed-Valent Uranium Oxides Using Total Reflection X-ray Fluorescence X-ray Absorption Near-Edge Spectroscopy," *Anal Chem* **89**(1), 871–876 (2017).

6. T.T. Böhlen et al., "The FLUKA Code: Developments and Challenges for High Energy and Medical Applications," *Nuclear Data Sheets* **120**, 211–214 (2014).

7. MCNP official web page, https://mcnp.lanl.gov/.

8. Roman Gromov, Argonne National Laboratory, Experimental Operations and Facilities Division, private communications.

9. Cumulative fission yields, https://www-nds.iaea.org/sgnucdat/c3.htm.

10. Krishichayan et al., "Fission product yield measurements using monoenergetic photon beams," *Phys Rev C* **100**, 014608 (2019).

11. ENDF-B cross-sections library, https://www-nds.iaea.org/exfor/endf.htm.

12. A. Inoue and T. Tsujino, "Dissolution rates of uranium oxide (U_3O_8) powders in nitric acid," *Industrial & Engineering Chemistry Process Design and Development* **23**(1), 122–125 (1984).

13. D.Y. Chung and E.H. Lee, "Kinetics of the Hydrolysis of Acetohydroxamic Acid in a Nitric Acid Solution," *J Ind Eng Chem* **12**, 962–966 (2006).

Chemical and Fuel Cycle Technologies Division
Argonne National Laboratory
9700 South Cass Avenue, Bldg. 205
Lemont, IL 60439-4854

www.anl.gov